European Journal of Pharmaceutical Sciences 192 (2024) 106652

Contents lists available at ScienceDirect

European Journal of Pharmaceutical Sciences

journal homepage: www.elsevier.com/locate/ejps

A pH-sensitive silica nanoparticles for colon-specific delivery and controlled release of catechin: Optimization of loading efficiency and in vitro release kinetics

Abdulsalam M. Kassem [a], May Almukainzi [b,*], Tarek M. Faris [b], Ahmed H. Ibrahim [a], Walid Anwar [a], Ibrahim A. Elbahwy [a], Farid R. El-Gamal [a], Mohamed F. Zidan [a], Mohamed A. Akl [a,c], Ahmed M. Abd-ElGawad [d], Abdelsamed I. Elshamy [e], Mohammed Elmowafy [a,f]

[a] Department of Pharmaceutics and Pharmaceutical Technology, Faculty of Pharmacy (Boys), Al-Azhar University, Nasr City 11751, Cairo, Egypt
[b] Department of Pharmaceutical Science, College of Pharmacy, Princess Nourah bint Abdulrahman University, P.O. Box 84428, Riyadh 11671, Saudi Arabia
[c] Department of Pharmaceutics, College of Pharmacy, The Islamic University, Najaf 54001, Iraq
[d] Department of Botany, Faculty of Science, Mansoura University, Mansoura 35516, Egypt
[e] Chemistry of Natural Compounds Department, National Research Centre, 33 El Bohouth St., Dokki, Giza 12622, Egypt
[f] Department of Pharmaceutics, College of Pharmacy, Jouf University, P.O. Box 2014, Sakaka, Saudi Arabia

ARTICLE INFO

Keywords:
Mesoporous silica nanoparticles
Catechin
pH-responsive drug delivery system
Colon targeting
Eudragit®-S100

ABSTRACT

Catechin is a naturally occurring flavonoid of the flavan-3-ol subclass with numerous biological functions; however, these benefits are diminished due to several factors, including low water solubility and degradation in the stomach's harsh environment. So, this study aimed to develop an intelligent catechin colon-targeting delivery system with a high loading capacity. This was done by coating surface-decorated mesoporous silica nanoparticles with a pH-responsive enteric polymer called Eudragit®-S100. The pristine wormlike mesoporous silica nanoparticles (< 100 nm) with high surface area and large total pore volume were effectively synthesized and modified with the NH_2 group using the post-grafting strategy. Various parameters, including solvent polarity, catechin-carrier mass ratio, and adsorption time, were studied to improve the loading of catechin into the aminated silica nanoparticles. Next, the negatively charged Eudragit®-S100 was electrostatically coated onto the positively charged aminated nanocarriers to shield the loaded catechin from the acidic environment of the stomach (pH 1.9) and to facilitate site-specific delivery in the acidic environment of the colon (pH 7.4). The prepared nanomaterials were evaluated using several methods, including The Brauner-Emmett-Teller, surface area analyzer, zeta sizer, Field Emission Scanning Electron Microscope, Powder X-Ray Diffraction, Fourier Transform Infrared Spectroscopy, Energy-Dispersive X-ray Spectroscopy, and Differential Scanning Calorimetry. In vitro dissolution studies revealed that Eudragit®-S100-coated aminated nanomaterials prevented the burst release of the loaded catechin in the acidic environment, with approximately 90% of the catechin only being released at colonic pH (pH > 7) with a supercase II transport mechanism. As a result, silica nanoparticles coated with Eudragit®-S100 would provide an innovative and promising approach in targeted nanomedicine for the oral delivery of catechin and related medicines for treating diseases related to the colon, such as colorectal cancer and irritable bowel syndrome.

1. Introduction

In recent years, there has been an upward trend of interest in developing functional or medicinal foods fortified with nutraceuticals in the food, pharmaceutical, and supplement industries (Pool et al., 2017). Nutraceuticals are dietary components with additional health advantages beyond those required by the body, such as the potential to reduce the risk of chronic illness or enhance human performance (Ditu et al., 2018; Alali et al., 2021). Catechin [CHT; Fig. 1] is a naturally occurring polyphenol substance of the flavonoid family, specifically the

* Corresponding author.
E-mail address: mkalmukainizi@pnu.edu.sa (M. Almukainzi).

https://doi.org/10.1016/j.ejps.2023.106652
Received 24 August 2023; Received in revised form 21 November 2023; Accepted 22 November 2023
Available online 25 November 2023

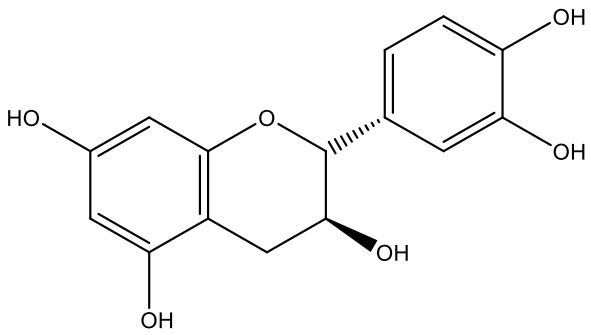

Fig. 1. Chemical structure of catechin.

flavan-3-ol subclass, abundantly found in strawberries, black grapes, cocoa, and, most particularly, green tea (Suner et al., 2022; Vong et al., 2022).

It may be utilized as a nutraceutical owing to its numerous significant biological activities, such as antioxidant, antimicrobial, and antiviral (Sistanipour et al., 2018). CHT also plays a vital role in preventing and treating diseases brought on by oxidative damage (Pritam et al., 2022; Jena et al., 2023). Moreover, it shows potential biological properties, such as anticancer, cardioprotective, anti-inflammatory, and neuroprotective effects (Mandel and Youdim, 2004; Kaur et al., 2017). In addition, it exhibits significant efficiency in enhanced lipid reduction on artery walls, protection against induced DNA damage, adhesion to cellular walls, and protection against microbial development on those walls (Kaur et al., 2017). Therefore, CHT is an interesting biomedical research subject for further investigation and potential drug development.

CHT's effectiveness depends on how much it reaches a specific place or tissue in a bioavailable form. Hence, the delivery method significantly impacts CHT's bioavailability (Athirojthanakij and Rashidinejad, 2023; Lv et al., 2023). Due to its ease of administration, the oral route is often the best choice for drug delivery applications. Unfortunately, its poor water solubility, decomposition based on enzyme activity and stomach acidity, low dissolution rate, limited absorption across intestinal membranes, and low oral bioavailability diminish these clinical values (Zhao et al., 2019; Dima et al., 2020; Subramanian, 2021; Blanco-Llamero et al., 2022). The two benzene rings in its chemical structure stand for the catechol and resorcinol groups, respectively; these groups are susceptible to changes in pH. Even at a relatively weak positive potential, the catechol groups undergo oxidation initially, followed by the resorcinol group. (Kaur et al., 2017).

Several studies have been conducted to overcome the limitations that impede the oral administration of CHT. This would include W/O reverse micelle microemulsion (Suner et al., 2022), chitosan (CS)-coated–PLGA–nanoparticles (Ahmad et al., 2020), alginate, pectin, and chitosan polymeric nanoparticles (Mondal et al., 2022), polylactic acid (PLA) and polyethylene glycol (PEG) nanoparticles (Singh et al., 2017), encapsulation cyclodextrins (Ho et al., 2017), liposome nanoparticles (Rashidinejad et al., 2014), cyclodextrins-liposomes nanosystem (Chen et al., 2014), and calcium alginate microparticles (Kim et al., 2016).

Mesoporous silica nanoparticles (MSNPs), a distinct family of inorganic materials, have recently attracted growing interest as an intelligent delivery system due to their unique properties, such as large surface area ($> 700\ m^2/g$), large pore volume, tunable pore diameter, and particle size, and physicochemical stability, as well as good biocompatibility and low toxicity (Ibrahim et al., 2020; Kankala et al., 2020; Zhang et al., 2022; Zhou et al., 2022; Elmowafy et al., 2023). For the amorphization of drug crystals, MSNPs are superior to prior nanosystems that employed polymers or surfactants by confining the drug particles in stiff nanoporous networks between 2–50 nm (Contreras et al., 2019; Elmowafy et al., 2023). In addition, porous silica materials are accessible to chemical alteration or polymer coating because of their free and germinal silanol groups (Wei et al., 2016; Kamarudin et al., 2013). It offers silica properties and added advantages, including enhancement of drug loading, cancer cell targeting, and extended medication release (Liu et al., 2011; Iraji et al., 2018).

Drugs that may be taken orally and delivered specifically to the colon for treating illnesses like inflammatory bowel disease, Crohn's disease, constipation, and colon cancer are the subject of extensive research (McCoubrey et al., 2023). Traditional methods use pH- (Sunoqrot and Abujamous, 2019; Cai et al., 2021; Xu et al., 2022; Zhang et al., 2023), time (Foppoli et al., 2019; Melocchi et al., 2021; Awad et al., 2022), or enzyme- (Krishnaiah et al., 2002; Rajan et al., 2013; Wijewantha et al., 2023) dependent systems to accomplish this selectivity. The pH-dependent drug release technique is one of the most effective strategies for colon-targeted administration through the oral route. This is achieved by coating the prepared nanoparticles with an acid-resistant polymer, which prevents the drug from being released prematurely in the stomach and upper gastrointestinal tract (GIT). The polymer undergoes dissolution when reaching the colon or large intestine, where the pH approaches neutrality, hence facilitating the release of the medication (Subudhi et al., 2015; Li et al., 2016; Dutta et al., 2022; da Fonseca Machado et al., 2023).

Pharmaceutical companies often use Eudragit® polymers, a class of commercially available methacrylic acid copolymers, to coat tablets and capsules with a film that delays drug release. Eudragit®-S100 (EUS-100) is the most suitable Eudragit® polymer for colon targeting, with a methacrylic acid to methyl methacrylate ratio of around 1:2 (Janrao et al., 2022). The insolubility of the polymer in acidic conditions may be attributed to the protonation of carboxyl groups present within the methacrylic acid moiety. In contrast, the side chains of the polymer remain uncharged. The carboxyl groups get ionized when exposed to neutral or basic pH levels. The polymer releases its payload as a consequence of the improvement in water solubility and the resulting negative repulsive charges between the carboxylate side groups (Sunoqrot and Abujamous, 2019; Rehman et al., 2021). As a result of their adaptability, Eudragit® polymers have found new uses beyond those of traditional film coating excipients, such as nanoparticle platforms for pH-dependent drug release.

Concerning the nanocarrier systems designed in this work, MSNPs were made by using the electrostatic interaction between inorganic silica materials and cetyl trimethyl ammonium bromide, a cationic surfactant, to guide the controlled polymerization of silica monomers. Following the creation of NH_2_MSNPs by grafting the surface hydroxyl moiety, EUS-100 coating was used to shield the drug-loaded nanoparticle, allow pH-controlled site-specific release, and modulate the bioadhesive characteristics of the resulting formulations for improved medication retention at the site of administration. The as-synthesized mesoporous system's physicochemical characteristics and dissolution pattern were then examined.

The literature lacks any details concerning using CHT-loaded, pH-gated MSNPs as a site-targeting and controlled release system. Thus, the goal of this research was to investigate the possibility of developing and evaluating a pH-sensitive polymer complex that could be generated around a CHT-loaded silica nanoparticle system to ensure that a therapeutically effective concentration of CHT reaches the distal parts of the GIT and improves local drug retention after administration, which could be accomplished by enhancing physicochemical properties and providing a controlled release pattern.

2. Materials and methods

2.1. Materials

Catechin with Product No.: PHR1963 was purchased from Merck KGaA (Darmstadt, Germany). Tetraethyl orthosilicate (TEOS, 98%), cetyl trimethyl ammonium bromide (CTAB), 3-aminopropyltriethoxysilane (APTES), triethanolamine (TEA), hydrochloric acid (HCl, 38 %),

absolute ethanol, methanol, dichloromethane (DCM), toluene and anhydrous N, N-dimethylformamide (DMF) were supplied by Sigma-Aldrich, Inc. (St. Louis, MO). EUS-100 was kindly provided by Evonik Röhm (GmbH, Germany). In addition, all the other solvents and chemicals were of analytical quality and used without any additional modification. In all experiments, the Milli-Q purification system supplied by EMD Millipore, Billerica (MA, USA) was utilized to generate ultrapure water with a specific resistivity of 18.2 M.cm at 25 °C.

2.2. Synthesis of Spherical MSNPs

Following the method reported by Elmowafy *et al.*, MSNPs were prepared using the cationic surfactant CTAB as a structure-directing agent and served as a template and TEOS as the silica source under the alkaline medium (Elmowafy et al., 2023). Specifically, the CTAB (3 g) and TEA (1.2 g) were mixed together in 60 mL of milli-Q water at 95 °C and stirred at 1000 rpm for 1 h. Next, 9 mL of TEOS was added at a rate of 1 mL/min. Before centrifugation at 12,000 rpm for 30 min, the developed silica nanoparticles were magnetically stirred for 60 min. To ensure the removal of any remaining reactants, a series of three washes were performed on the collected solid nanomaterials using milli-Q water and anhydrous alcohol. The as-synthesized nanoparticles were refluxed three times at 80 °C for 12 h in a 50: 1 (v/v) ethanol and hydrochloric acid mixture to get rid of any remaining surfactants. Subsequently, the mixture was centrifuged and subjected to three rounds of washing using milli-Q water and 100 % ethanol consecutively. The surfactant-free formulation (MSNPs) was created by subjecting it to vacuum drying at a temperature of −50 °C for a duration of 24 h.

2.3. Synthesis of NH_2–Modified MSNPs

The surface of MSNs was functionalized with aminopropyl groups using the post-grafting method reported previously (Raza et al., 2021) with minor modification. Briefly, MSNPs (1 g) were degassed at 150 °C for 1 h to remove the adsorbed gases and water, followed by dispersion in 100 mL anhydrous toluene by sonication (Soniclean Pty. Ltd., Japan) for 15 min. APTES was added dropwise to the prepared mixture and mixed gently at 500 rpm at 60℃ for 1 h. The mixture was then heated to 125 °C and left to reflux for 24 h in a nitrogen-filled environment. After centrifugation at 15.000 rpm for 15 min and washing with toluene and ethanol thrice, respectively, aminated MSNPs were dried under a vacuum at −50 °C for 24 h. The resulting products were denoted NH_2–MSNPs.

2.4. Catechin loading

CHT was loaded into nanoparticles at w/w ratios of 1:1, 1:2, 1:3, and 1:4 using the solvent evaporation process. After degassing at 150 °C for 1 h, a suitable amount of NH_2–MSNPs was dispersed in 5 mL of concentrated CHT solution. In order to examine the effect of solvent type on CHT loading, 20 mg of CHT was dissolved in 5 mL of DMF and DCM mixture at different ratios (v/v) of 3:1, 3:2, 1:1, 1:2, 1:3, and 1:4 in a hermetically sealed container that was held at 37 °C in the dark while being stirred at 100 rpm. To find out how loading duration impacts adsorption efficiency (AE), the dispersion was shaken for 4, 8, 10, 12, 24, and 48 h. Following the evaporation of the samples to a volume of 1 mL, which resulted in a potentially increased drug concentration gradient, the samples were centrifuged and subsequently subjected to three cycles of washing using deionized water and the corresponding loading solvent to remove the unadsorbed CHT, followed by drying under vacuum conditions.

After evaporating the samples down to 1 mL (resulting in a potentially increased drug concentration gradient), they were centrifuged and washed with deionized water and the matching loading solvent several times before being dried under a vacuum. The resulting nanomaterials were designated as NH_2–MSNPs/CHT. CHT AE was determined by collecting the supernatant from each phase of the experiment at 280 nm (Suner et al., 2022; Hu et al., 2021; Prakashkumar et al., 2021; Yaneva et al., 2021; Shim et al., 2019) utilizing a UV–visible spectrophotometer (Shimadzu UV-1800, Kyoto, Japan). The calibration curve of CHT absorbance at 280 nm (characteristic of the flavan-3-ol structure) vs concentration in ultra-pure water was used to quantify the amount of CHT that was absorbed by the nanoparticles ($r^2 = 0.99979$, $y = 0.01285\ x + 0.00221$). The following formula may be used to determine the AE:

$$\textbf{\textit{AE}}\ (\%) = \frac{(\textbf{\textit{Total amount of CHT added}} - \textbf{\textit{Unabsorbed amount in supernatant}})}{\textbf{\textit{Total amount of CHT added}}} \textbf{\textit{x}}\ 100 \quad (1)$$

However, the following equation was used to calculate the CHT loading:

$$\textbf{\textit{CHT loading}}\ (\%) = \frac{\textbf{\textit{weight of the adsorbed CHT}}}{(\textbf{\textit{weight of adsorbed CHT}} + \textbf{\textit{weight of nanoparticles}})} \textbf{\textit{x}}\ 100 \quad (2)$$

The optimized conditions that produced the highest CHT adsorption and loading capacity were also used to create a CHT complex with unfunctionalized nanoparticles as a reference model (MSNPs/CHT).

2.5. Eudragit®-S100 Coating

The rotary evaporation method was utilized to generate NH_2–MSNPs coated with EUS-100 loaded with CHT. After dispersing 100 mg of NH_2–MSNPs/CHT in 2 mL of methanol, 2 mL of pH-sensitive polymer EUS-100 (10 wt%) was added drop-by-drop. Following sonication in a water bath for 30 min, methanol was evaporated at 40 °C using a rotary evaporator [Stuart rotary evaporator (RE300)] equipped with a vacuum pump (RE3022C, UK), and eventually, the resulting particles were noted as NH_2–MSNPs/CHT@EUS-100. Noticeably, the coating process with pH-sensitive polymer, EUS-100, was repeated thrice. NH_2–MSNPs@EUS-100 is used throughout the manuscript to refer to the EUS-100-coated nanoparticles without loading.

2.6. Characterization

2.6.1. Nitrogen physisorption analysis

From N_2 adsorption-desorption isotherms recorded at −196 °C using BELsorp- Max (BEL, Japan), the samples' specific surface area (SSA), pore size, and total pore volume were calculated. Before analyses, the silica nanoparticles were outgassed overnight under a vacuum at 50 °C. The Brunauer-Emmet-Teller (BET) technique was used, using experimental points at a relative pressure of $P/P_0 = 0.05–0.2$, to compute the specific surface area (SSA). The Barrett-Joyner-Halenda (BJH) approach was used to estimate the typical pore size in the adsorption branch of the isotherms. The total pore volumes were computed after calculating the quantity of N_2 adsorbed at a relative pressure of 0.9814.

2.6.2. High-Resolution Transmission Electron Microscopy (HR-TEM)

The surface morphology of the produced MSNPs and NH_2–MSNPs/CHT@EUS-100 was investigated using 200 kV HR-TEM (JEM-1011; JEOL, Tokyo, Japan). Sonication was first used to suspend MSNPs in 100 % ethyl alcohol for 10 min. The obtained samples were then gently placed on a carbon-coated copper grid. Once the specimen was dried at room temperature, it was placed on a grid and photographed at various magnifications using the microscope.

2.6.3. Field-Emission Scanning Electron Microscopy (FE-SEM)

Pure MSNPs and NH_2–MSNPs/CHT@EUS-100 were subjected to FE-SEM to inspect the particle size and morphology using an SEM apparatus (Bruker Nano GmbH, company German origin, type vertex 5600LV SEM). The samples were embedded in resin, and the other side was afterwards roughly polished to provide a flat surface to facilitate the sample's easy adhesion to the plate specimen. Prior to analysis at various magnifications, the sample's powder was treated with carbon to potentiate the electrical conductivity.

2.6.4. Elemental Analysis and Energy-Dispersive X-ray Spectroscopy

A study was conducted to detect the presence of carbon (C), nitrogen (N), oxygen (O), and silicon (Si) in pristine (MSNPs) and surface-decorated nanoparticles (NH_2–MSNPs and NH_2–MSNPs@EUS-100). This was achieved through the use of energy-dispersive X-ray spectroscopy (EDX) analysis and scanning transmission electron microscopy (STEM). The analysis was performed on a JEM-2100 F (URP) instrument operating at 200 kV, equipped with a Dry SD30GV Detector.

2.6.5. Mean Particle Size, Polydispersity Index (PDI), and Zeta Potential (ζ)

Dynamic light scattering (DLS) was used to evaluate the mean diameter, PDI, and zeta potential of MSNPs, NH_2–MSNPs, NH_2–MSNPs/CHT, NH_2–MSNPs@EUS-100, and NH_2–MSNPs/CHT@EUS-100 utilizing a Malvern® Zetasizer Nano Zs 90 (Malvern® Instruments Limited, Worcestershire, UK). After proper dilution with ultrapure water, the freshly produced silica samples silica were analyzed at 25 °C with a 90° scattering angle; the data is presented as the mean ± standard deviation (SD) of three independent experiments.

2.6.6. Thermogravimetric Analysis (TGA)

The thermal behaviour and percentage of weight loss due to an increased temperature were recorded for CHT, EUS-100, MSNPs, NH_2–MSNPs, NH_2–MSNPs/CHT, and NH_2–MSNPs/CHT@EUS-100 using Simultaneous DSC-TGA/DTA equipment (Discovery, SDT 650, USA). All measurements were conducted in a nitrogen atmosphere (10 mL/min) with a sample mass of approximately 5 mg at a temperature rate of 10 °C/min from ambient temperature to 800 °C.

2.6.7. Differential Scanning Calorimetry (DSC)

Various nanoparticles' phase transitions and characteristics were investigated using a Shimadzu DSC TA-50 ESI-DSC instrument (Tokyo, Japan). This included CHT, EUS-100, MSNPs, NH_2–MSNPs, NH_2–MSNPs/CHT, and NH_2–MSNPs/CHT@EUS-100. The thermal scan of the fresh samples, each weighing about 5 mg, was carried out at a scanning speed of 10 °C/min from 25 to 350 °C with a nitrogen flow of 50 mL/min.

2.6.8. Powder X-Ray Diffraction (PXRD)

Nanoparticle samples' degrees of crystallization and amorphization were determined using a Shimadzu XD-610 X-ray diffractometer (Tokyo, Japan) outfitted with a Cu Kα as a radiation supplier (40 kV × 20 mA). The angular scan was performed at a rate of 1 °/min, ranging from 10° to 70° with a diffraction angle of 2-theta with a step size of 0.02 (4 s/step).

2.6.9. Fourier Transform Infrared Spectroscopy (FT-IR)

The chemical composition of the identical samples assessed by DSC and PXRD tests in addition to NH_2–MSNPs@EUS-100 formulation was analyzed by means of FT-IR spectroscopy using a Jasco FT-IR spectrophotometer (FT-IR-8400 spectrophotometer; Shimadzu). A precise mixture of 100 mg of KBr and 2 mg of the sample was compressed using a press unit (Mini Press, MP-1; JASCO Co., Tokyo, Japan). Each FT-IR was scanned a hundred times at 4 cm^{-1} resolution over the 4000–400 cm^{-1} wavenumber region.

2.6.10. In vitro pH-responsive drug release

The in vitro pH-sensitive release studies of pure CHT, MSNPs/CHT, NH_2–MSNPs/CHT, and NH_2–MSNPs/CHT@EUS-100 were carried out using a USP apparatus II (ERWEKA, DT 600, Heusenstamm, Germany) operated at 100 rpm and 37 ± 0.5 °C. According to the United States Pharmacopeia (USP), the "universal buffer" was used to determine the pH-responsive drug release capabilities of the EUS-100 coated silica nanoparticles that were loaded with CHT (Qu et al., 2021). Typically, 500 mL of the prepared universal buffer was employed to disperse 20 mg of the medication and an equivalent amount of drug-loaded nanosystems. A 1:1 volume ratio of phosphate buffer and acetic acid (0.05 M) was used to create a universal buffer (pH 1.9). To simulate the gradual pH shift of the GIT, the pH of the release medium was changed to 4.5 and 7.4 using 8 M of NaOH at 2- and 5 h time intervals. At specific time intervals, 2 mL of the release medium was withdrawn and replaced with a new release medium. To eliminate any silica particles from the withdrawn samples, they were first centrifuged and then passed through a 0.2 syringe filter, and the drug concentration in the resulting supernatant was determined spectrophotometrically at λ_{max} of 280 nm. The average and SD were calculated from three independent runs.

2.6.11. In-vitro drug release kinetics

In order to evaluate the mechanism of CHT release from the produced silica nanoparticle, five distinct kinetic models were considered for their ability to fit the experimental results with the highest regression coefficient, including the zero-order model (Eq. (3)), the first-order model (Eq. (4)), the Higuchi model (Eq. (5)), the Hixson-Crowell model (Eq. (6)) and the Korsmeyer-Peppas model (Eq. (7)). The drug release parameters were computed using mathematical models according to the following equations:

$$\boldsymbol{Q_t} = \boldsymbol{K_0 . t} \tag{3}$$

$$\ln(100 - \boldsymbol{Q_t}) = \ln 100 - \boldsymbol{K_1 . t} \tag{4}$$

$$\boldsymbol{Q_t} = \boldsymbol{K_H . t^{1/2}} \tag{5}$$

$$(100 - \boldsymbol{Q_t})^{1/3} = (100)^{1/3} - \boldsymbol{K_{HC} . t} \tag{6}$$

$$\boldsymbol{Q_t} = \boldsymbol{K_{KP} . t^n} \tag{7}$$

Where Q_t denotes the quantity of drug that has dissolved in specific time t, and Q_0 denotes the quantity of medication that was initially present in the nanoparticles. K_0, K_1, K_h, $K_{HC,}$ and K_{KP} refer to the constant for the

zero-order rate, the constant for the first-order rate, the constant for the Higuchi release rate, the constant for the Hixson-Crowell rate equation, the constant for the Korsmeyer-Peppas model equation, respectively. The Korsmeyer-Peppas kinetic model was used to derive the release or diffusion exponent (n). The Korsmeyer-Peppas model's n exponent was estimated using 60 % cumulative CHT release data. The Fickian diffusion was explained when the value of n was less than 0.43, and the anomalous mechanism (non-Fickian) was reported when the value of n was between 0.0.43 and 0.85. According to Fick's laws, the two different forms of diffusion, Fickian and non-Fickian diffusion, cannot coexist simultaneously. In contrast to Fickian-diffusion, which has no boundaries, non-Fickian-diffusion has a clear border dividing the loaded drug region (Chourasiya et al., 2016). Supercase II transport is indicated by values of $n \geq 0.85$, wherein drug release is exclusively controlled by polymer swelling and relaxation (Sunoqrot and Abujamous, 2019).

2.6.12. Short-term stability studies

The NH_2–MSNPs/CHT@EUS-100 was carefully encased inside a hermetically sealed vessel made of amber-yellow glass. Subsequently, it was positioned within a desiccator maintained at a temperature of 25 °C and a relative humidity of 75 %. This controlled environment was achieved by using a saturated solution of NaCl. The nanoparticles were subjected to sampling at four different time points: 0, 1, 2, and 3 months. These samples were then assessed for several parameters, including particle size, PDI, zeta potential, and CHT AE.

2.7. Analytical statistics

The results are expressed as the mean ± standard deviation of n independent experiments and analyzed with GraphPad Prism software (version 8.00; GraphPad Software, San Diego, California) using one-way ANOVA. P values less than 0.05 were statistically significant.

3. Results and discussion

3.1. Preparation of silica nanomaterials

The current study explores a pH-responsive strategy for developing silica nanoparticles suitable for targeting CHT in the lower GI tract. The MSNPs are prepared by agglomeration and condensation of silica-cationic surfactant micelles (electrostatic interaction) in the presence of a surface capping ligand (TEA). The tetraethyl orthosilicate (TEOS) experienced hydrolysis upon contact with water, forming a silica monomer with a negative charge. Subsequently, this negatively charged silica monomer was encapsulated by surfactant micelles carrying a positive charge, forming composites consisting of silica-surfactant micelles. The hydrolysis reaction was expedited by adding triethylamine (TEA), a substitute for a basic catalyst (Lv et al., 2016). The developed

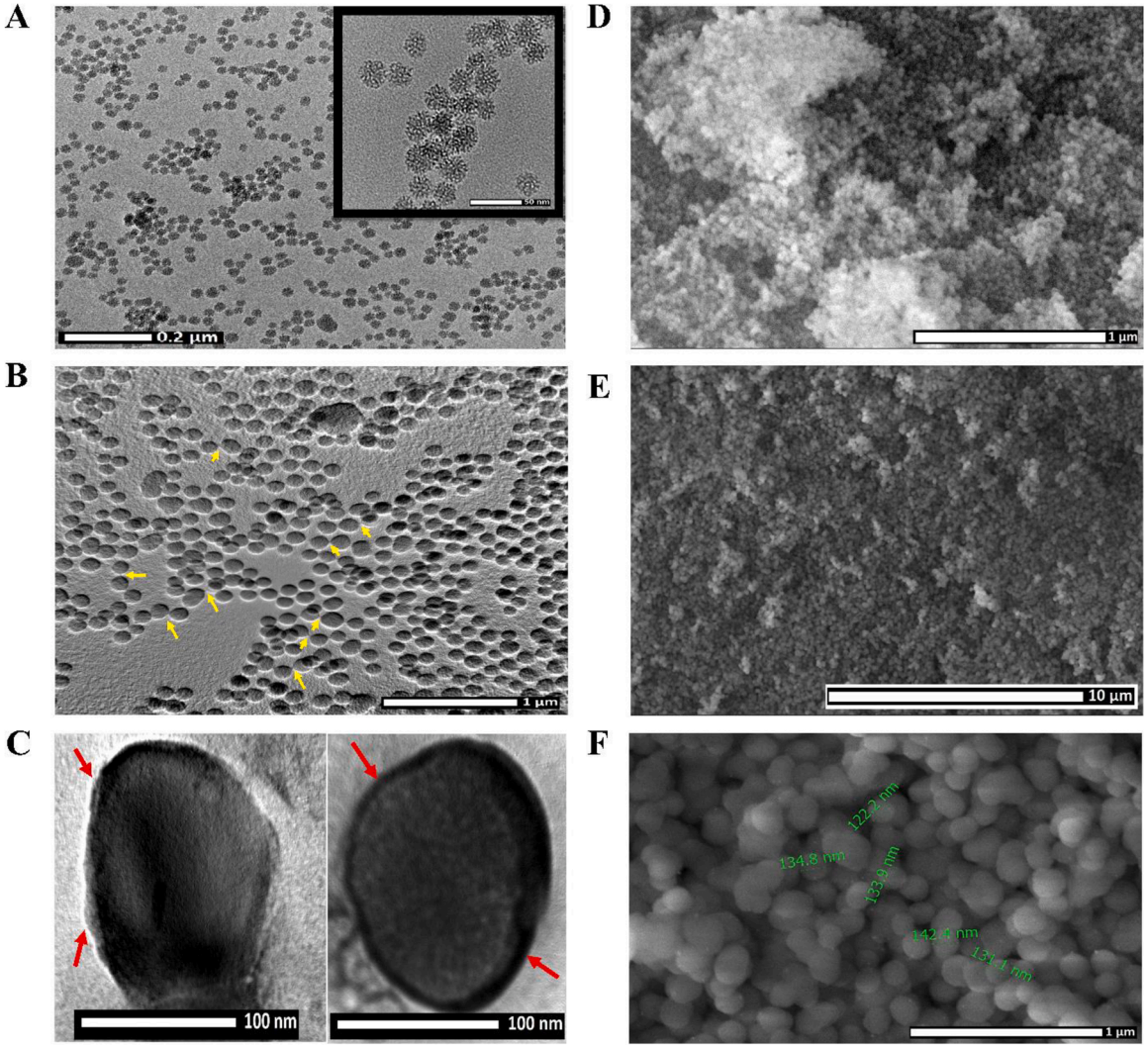

Fig. 2. TEM of **(A)** bare MSNPs and **(B & C)** NH_2–MSNPs/CHT@EUS-100. **(D)** Scanning electron microscopy of pure MSNPs and **(E & F)** NH_2–MSNPs/CHT@EUS-100. The operations of capturing the HR-TEM images were carried out at 200 kV with different magnification powers.

composites started aggregating and producing the nuclei essential for particle growth (Feng et al., 2014). The excess unreacted CTAB is eliminated using a highly concentrated hydrochloric acid and anhydrous ethanol solution. The amino group was then grafted onto the surface of MSNPs using a post-grafting approach, and CHT was then physically loaded into NH_2_MSNPs using a solvent evaporation procedure. Finally, coating the surface-modified nanocarrier with EUS-100 through the ionic interaction, which generates pH-gated nanoparticles, allowed the loaded aminated nanosystem to be transported to the colon.

3.2. Morphological, elemental, and structural analysis

Electron microscopy was used to examine the size and structural properties of the produced MSNPs, as seen in the TEM and SEM micrographs (Fig. 2). As shown in the TEM image (Fig. 2A), the generated MSNPs had a diameter of about 35 nm, were non-aggregated, monodispersed, and almost spherical, with a disordered, wormlike channel topology. It was clear to notice the wormlike mesochannels dispersed randomly across the whole particle. The TEM images of the NH_2_MSNPs/CHT@EUS-100 (Fig. 2 (B & C)) clearly demonstrate that the nanomaterials with coating have a more pronounced black colour than the untreated MSNPs. Furthermore, wormlike mesochannels are completely lacking across the whole particle. In addition, the observation of the bridging phenomena (yellow arrows) and the existence of a thin coating layer (red arrows) on NH_2_MSNPs/CHT@EUS-100 provide compelling evidence of the effective polymer coating process on the silica particles. The findings are consistent with the previously published results (Raza et al., 2021).

The surface shape of the MSNPs is evaluated by FE-SEM, as illustrated in Fig. 2D. As the FE-SEM photomicrograph shows, MSNPs revealed the typical uniform sphere reflections, and all seemed to be around the same size, corresponding to the monodispersed spherical form seen in the TEM images. Due to its small size, the latter measure is ideal for nanomedicine goals and suited for covering with a polymeric layer (Popova et al., 2018). The SEM analysis of NH_2_MSNPs/CHT@EUS-100 (Fig. 2 (E & F)) revealed a spherical structure with relative roughness and aggregation, which may be attributed to the polymer film. The observed increase in darkness and

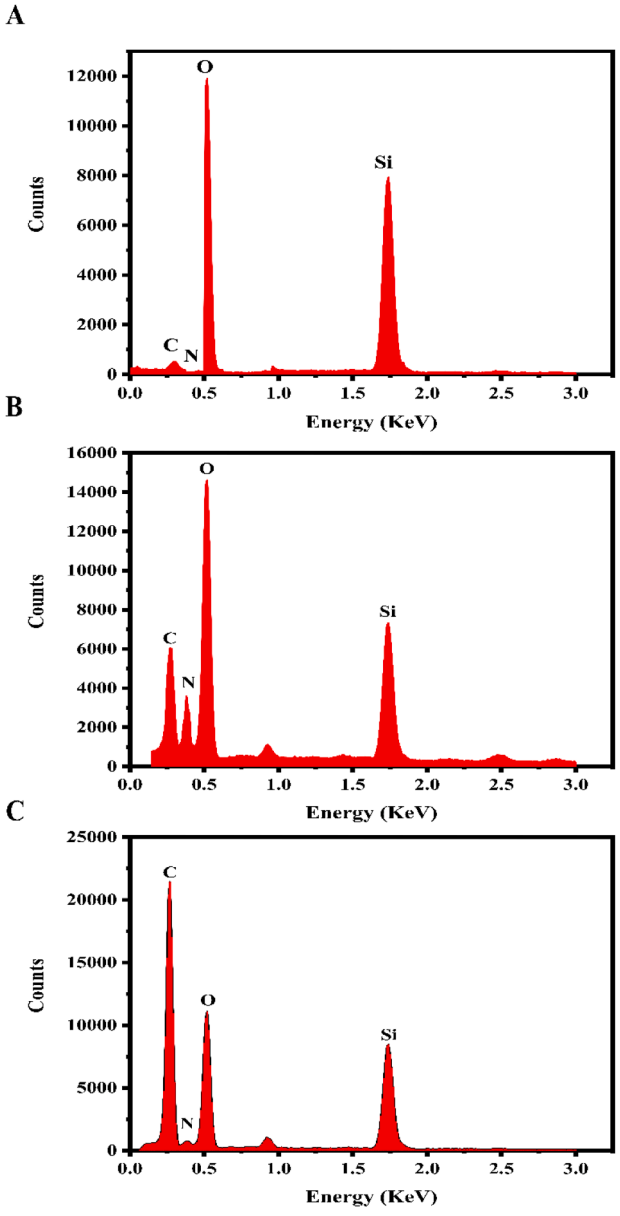

Element	Wt%
O	35.83
Si	63. 26
C	0.91
N	0.00

Element	Wt%
O	28.37
Si	41. 94
C	22.45
N	7.24

Element	Wt%
O	19.07
Si	21.41
C	59.52
N	0.00

Fig. 3. (A) STEM-EDX images of MSNPs, NH_2_MSNPs, and NH_2_MSNPs@EUS-100.

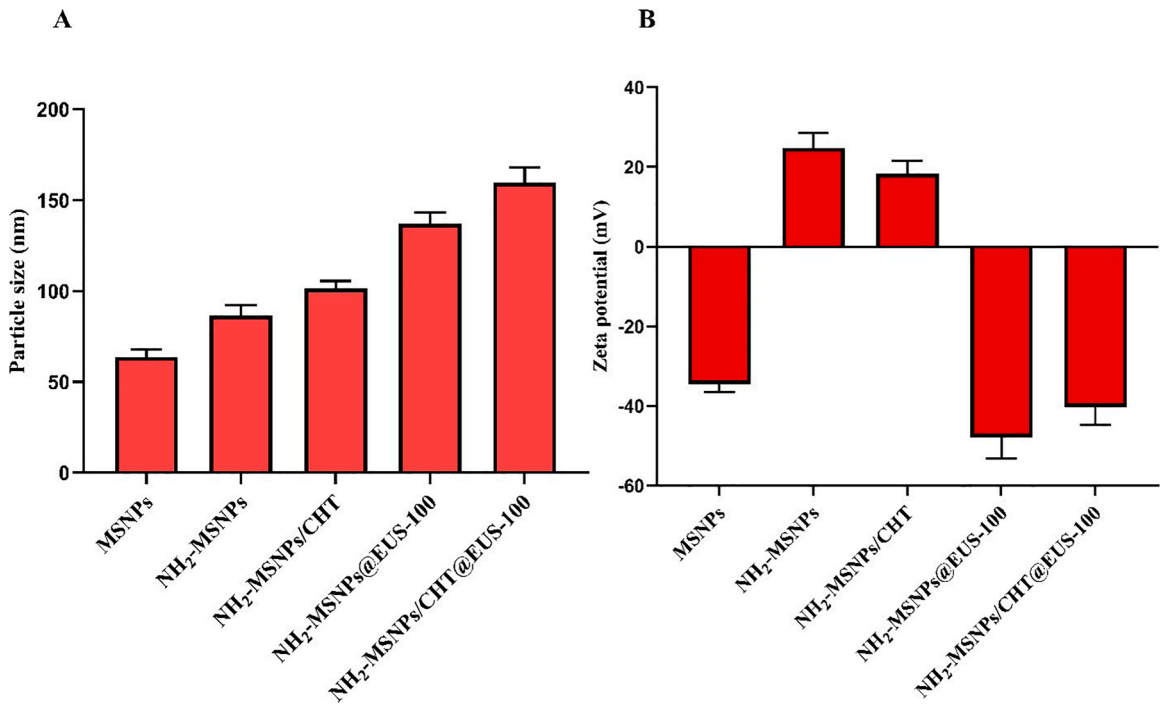

Fig. 4. **(A)** The mean particle diameter and **(B)** zeta potential of MSNPs, NH_2-MSNPs, NH_2_MSNPs/CHT, NH_2_MSNPs@EUS-100 and NH_2_MSNPs/CHT@EUS-100. The analysis was conducted at 25°C with a 90° scattering angle; the data is presented as the mean ± SD, (n = 3).

particle size of coated silica nanoparticles, in comparison to pure silica nanoparticles, suggests the effective encapsulation and coating of the synthesized nanomaterials, as plainly demonstrated in the TEM pictures.

Fig. 3 illustrates the STEM-EDX spectra and the quantitative elemental composition of the samples. In the case of bare MSNPs (Fig. 3A), it was discovered that the majority of the composition comprised SiO_2, with elemental composition of Si (63.26 %) and O (63.26 %). A negligible quantity of carbon was detected (< 1 %), indicating a high purity level in the manufactured nanoparticles (Yuvakkumar et al., 2014; Dubey et al., 2015). The data shown in Fig. 3B clearly indicates that both nitrogen (7.24 %) and carbon (22.45 %) were introduced after APTES functionalization. This is likely owing to the incorporation or anchoring of aminopropyl groups onto the OH group of the bare MSNPs. The initial composition of MSNPs comprised a significant proportion of silicon and oxygen. However, after the reaction with APTES, there was a notable reduction in the percentage of both silicon and oxygen, recording 41.94 and 28.37 %, respectively. This drop may be attributed to the introduction of nitrogen and a higher concentration of carbon in the resulting material, which is in line with prior findings reported by Jia et al. (2014) and He et al. (2022).

The examination of STEM-EDX verified the comprehensive synthesis of NH_2_MSNPs@EUS-100 spectra. Fig. 3C illustrates a notable rise in the carbon content (59.31 %) and a subsequent decline in the silicon (21.41 %) and oxygen (19.7 %) percentages throughout the NH_2_MSNPs@EUS-100 nanoparticles, mainly attributed to the abundance of methacrylic acid moieties found in EUS-100. Additionally, it was clear that nitrogen had totally missed out on the synthesized NH_2_MSNPs@EUS-100. The observed increase in carbon content and the lack of nitrogen in NH_2-MSNPs@EUS-100 further prove that the nanoparticles have been effectively and thoroughly functionalized with a substantial grafting percentage of EUS-100 (Mei et al., 2012).

Fig. 4A depicts the particle diameter records of several MSNPs. The average size of MSNPs, NH_2_MSNPs, NH_2_MSNPs/CHT, NH_2_MSNPs@EUS-100, and NH_2_MSNPs/CHT@EUS-100 were 63.86, 86.48, 101.36, 137.23 and 159.67 nm, respectively. The size of NH_2_MSNPs, NH_2_MSNPs/CHT, and NH_2_MSNPs@EUS-100 significantly elevated compared to the bare MSNPs ($P < 0.05$), indicating effective surface grafting, CHT loading, and EUS-100 coating on the surface of aminated MSNPs via electrostatic interaction, which was supported by the subsequent studies. From these results, NH_2_MSNPs/CHT@EUS-100 is still in the nanosize range (< 200 nm) with a narrow size distribution (< 0.3). As explained by smaller PDI values (Table 1), all the MSNPs exhibited a high uniformity in their diameter. The presence of TEA, which was supposed to serve as a surface-capping ligand to limit aggregation of the produced MSNPs and impede particle diameter development, may be responsible for the small size and narrow distribution.

As predicted, the particle size recorded by electron microscopy was smaller than those observed via dynamic light scattering (DLS). Since the DLS data provides the hydrodynamic radius (R_H) of the particles, including the center of the particle and any connected layer surrounding it, this could be responsible for this observation. In contrast, TEM relies on a sample's particle number after thoroughly drying; the findings result from electron scattering during sample irradiation. The obtained

Table 1
BET surface area, pore volume, mean pore diameter, and PDI of the prepared silica nanoparticles.

Sample	Pore width (W_{BJH}) (nm)	Total pore volume (V_T) (cm^3/g)	BET surface area (S_{BET}) (m^2/g)	PDI
MSNPs	2.95	1.38	945.12	0.08 ±0.03
NH_2_MSNPs	2.24	1.02	781.67	0.06 ± 0.06
MSNPs/CHT	1.69	0.72	493.27	0.11 ± 0.07
NH_2_MSNPs/CHT	0.86	0.31	194.16	0.17 ± 0.07
NH_2_MSNPs/CHT@EUS-100	0.23	0.11	23.62	0.23 ± 0.09

results were consistent with the observations published by Ibrahim et al. (2020).

The nanoparticles' surface electric charge was observed using zeta potential analysis (Joudeh and Linke, 2022). Fig. 4B displays the zeta potential of several nanomaterial samples as determined by the Malvern Zeta Sizer. The pure MSNPs showed negatively charged zeta potential (ZP = −34.52 mV) due to the surface silanol group (Badihi et al., 2022). On the other hand, the NH_2_MSNPs had a much more positive charge (ZP = +24.79 mV) because of the enormous number of aminopropyl groups linked to the free MSNPs surface by conducting electrostatic force. Changing the surface charge of silica nanoparticles from negative to positive value demonstrates that the amino group is successfully incorporated during the functionalization of pure nanomaterials (Rahaman et al., 2023). Zeta potential's negative charge was restored after coating the NH_2_MSNPs with EUS-100 but at a higher value of about −47.82 mV, demonstrating effective coating of positively charged particles with negatively charged polymer.

The absolute value of zeta potential for the loaded samples (NH_2_MSNPs/CHT and NH_2_MSNPs/CHT@EUS-100) was slightly reduced (+18.38 and −40.25 mV, respectively) as compared to the unloaded nanoparticles (NH_2_MSNPs and NH_2_MSNPs@EUS-100), but the changes were not statistically significant ($P > 0.05$). This might be justified by the partial deposition of CHT as a neutral chemical compound on the surface, which may mask the surface charge. Specifically, CHT includes both basic and acidic functional groups. As a result, the solution's pH will affect CHT's total potential. CHT will mainly exist in its protonated state and have a positive charge at a pH lower than its pKa value. CHT will predominantly exist in its deprotonated form and have a negative charge at a pH above its pKa value. CHT will be in a neutral state at its pKa value. Since DMF and DCM are nonpolar solvents, they shouldn't trigger the ionization of CHT in this work; hence, the molecule should exist as a neutral structure, and ultimately, the surface deposition could slightly conceal the surface electrical charge.

3.3. BET and BJH analysis

Nitrogen (N_2) adsorption-desorption isotherm measurements were used to determine the surface area and pore size distribution of various nanoparticle samples. Pore size distribution curves and nitrogen absorption-adsorption isotherms for parent MSNPs, NH_2_MSNPs, MSNPs/CHT, NH_2_MSNPs/CHT and NH_2_MSNPs/CHT@EUS-100 at low temperatures are presented in Fig. 5. Fig. 5A confirms the mesoporous character of the prepared nanoparticles samples by showing type-IV isotherms for both the unmodified (MSNPs) and amino-modified (NH_2_MSNPs) particles, as reported by the International Union of Pure and Applied Chemistry (IUPAC). The BET surface area of pure particles is 945.12 m^2g^{-1}, larger than the surface area of NH_2_MSNPs, which is decreased to 781.67 m^2g^{-1} due to amino silane binding, indicating the successful surface modification (Table 1). After drug loading, the particles' surface area further lowers to 493.27 m^2g^{-1} (MSNPs/CHT) and 194.16 m^2g^{-1} (NH_2_MSNPs/CHT). The aforementioned outcomes showed that CHT had been loaded into the pores of nanoparticles, filling the nanocarrier's most porous area. The polymeric-coated particles (NH_2_MSNPs/CHT@EUS-100) showed a significantly reduced BET surface area of 23.62 m^2g^{-1} ($P < 0.05$) due to the polymer chain's coverage. The N_2 adsorption-desorption isotherm studies validated the successful coating, which showed that the mesoporous pore structure of NH_2_MSNPs/CHT@EUS-100 was obstructed.

The Pore size of NH_2_MSNPs was reduced to 2.24 nm by the attachment of functionalized silanes to the mesopore surface, whereas it was 2.95 nm in the parent nanomaterials (Fig. 5B), which was estimated using the BJH method's adsorption branch of the isotherm. The hysteresis loop maintained its same form despite a decrease in the quantity of nitrogen adsorbed. This indicates that the post-synthesis process had little effect on pore morphology (Zhang et al., 2010). In addition, following amino substitution, the pore volume of particles dropped from 1.38 to 1.02 cm^3/g^{-1}. Likewise, as a consequence of CHT adsorption onto silica nanoparticles, the pore size diminished to 1.69 nm (MSNPs/CHT) and 0.86 nm (NH_2_MSNPs/CHT).

Moreover, the pore volume of MSNPs/CHT and NH_2_MSNPs/CHT dropped to 0.72 and 0.31 cm^3/g^{-1}, respectively (Table 1). The smallest pore width and volume were identified in drug-coated particles (NH_2_MSNPs/CHT@EUS-100), which were 0.23 nm and 0.11 cm^3/g^{-1}, respectively. These findings corroborate the results of the BET tests and provide evidence for grafting, adsorption, and polymer coating efficiency. As was previously indicated, this assumption was demonstrated by a significant drop in all of the measurable metrics of the BET and BJH approaches.

3.4. Adsorption Efficiency (AE) and loading capacity of CHT

A solvent evaporation strategy was utilized to incorporate CHT into the as-prepared nanosystems, and the effects of varying DMF: DCM volume ratios, CHT: NH_2_MSNPs mass ratios, and CHT adsorption times on loading % and AE % were investigated.

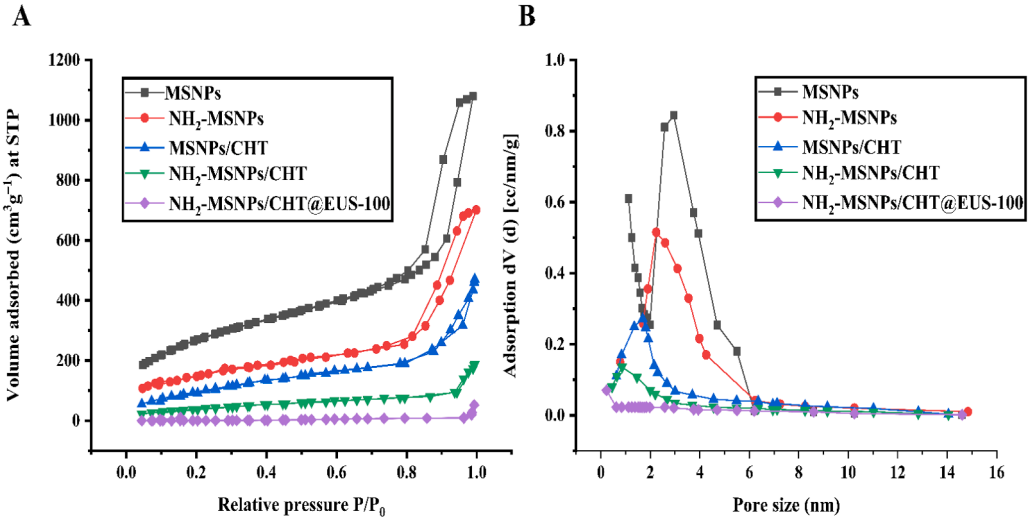

Fig. 5. **(A)** Nitrogen adsorption-desorption isotherm was conducted at a relative pressure of P/P0 = 0.05–0.2, and **(B)** corresponding Barrette-Joyner-Halenda (BJH) pore size distribution curves of MSNPs, NH_2_MSNPs, MSNPs/CHT, NH_2_MSNPs/CHT and NH_2_MSNPs/CHT@EUS-100.

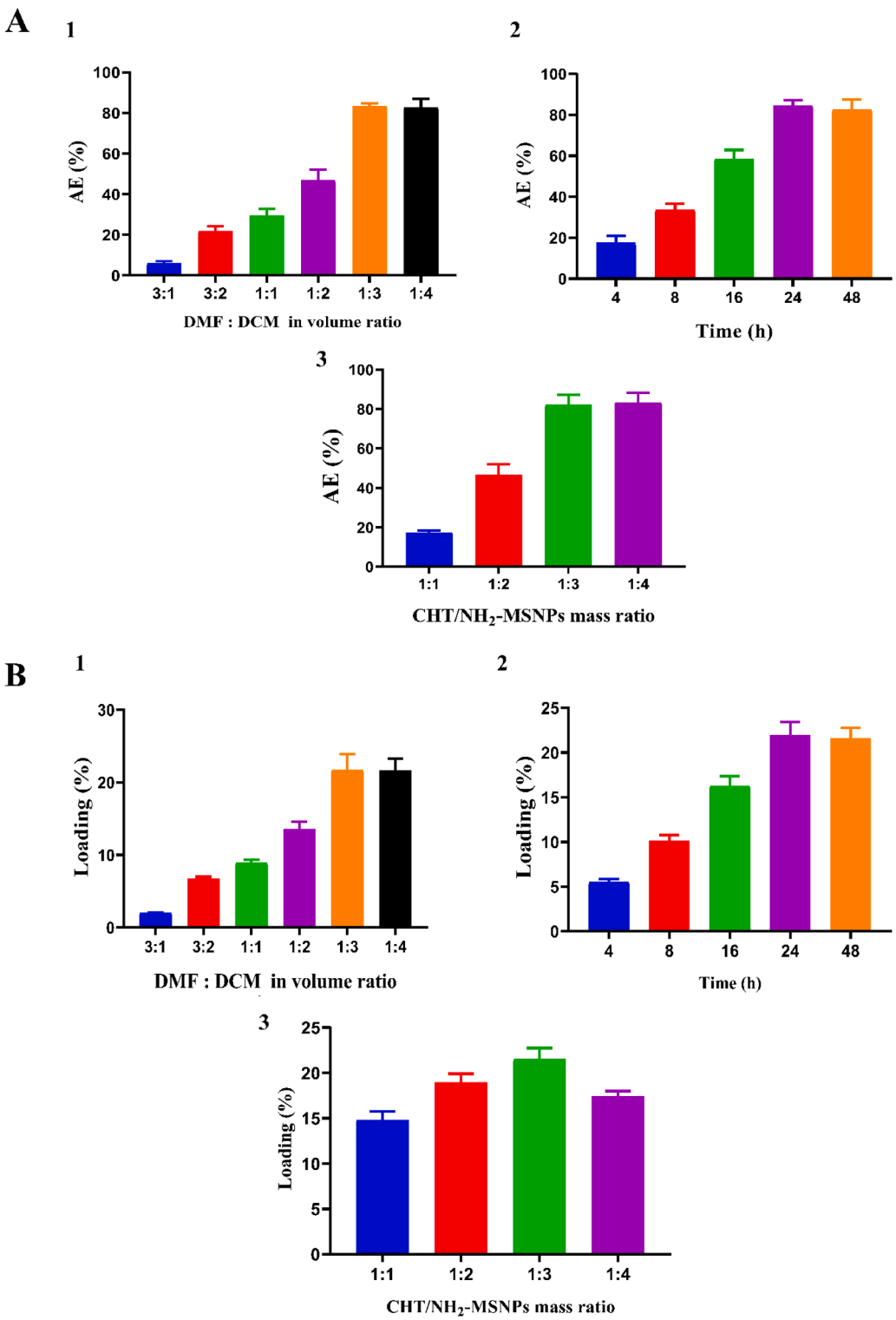

Fig. 6. The catechin adsorption efficiency and loading % of NH_2–MSNPs at **(A & D)** different volume ratios of DMF-DCM solvent mixture, **(B & E)** adsorption periods, and **(C & F)** catechin-carrier mass ratio, respectively.

3.4.1. Effect of solvents

A solvent mixture of two organic solvents (DMF and DCM) with different polarity indices and dielectric constants was utilized at a constant ratio of 1:3 (w/w) of CHT to NH_2–MSNPs to test whether the as-prepared nanoparticles could successfully load CHT. As seen in Fig. 6 (A1 & B1), the CHT AE and loading percentages were significantly enhanced ($P < 0.5$) by increasing the DCM portion ratio in the solvent mixture. The AE and loading percentages were highest (83.41 % and 21.75 %, respectively) at the 1:3 v/v ratio of the DMF-DCM mixture. Contrarily, the lowest values of AE (6.15 %) and loading capacity (2 %) were recorded when the DMF: DCM ratio was reversed to a 3:1 v/v ratio. The CHT AE and loading capacity did not change significantly ($P > 0.05$) when the DMF-DCM ratio was increased from 1:3 to 1:4 (v/v%). This difference is likely owing to the polarity of the solvent. The solvent competes with CHT for adsorption on the nanocarrier when the polarity index of the solvent mixture is boosted by increasing the DMF portion

(dielectric constant = 36.71, polarity index = 6.4) (Saxena et al., 2023; Le Guével et al., 2022; Lin et al., 2022; Kalhori et al., 2022). When the polarity index of the solvent combination gets lower by adding more DCM, the solvent has a lower chance of competing with CHT for adsorption on the nanocarrier. (dielectric constant = 8.93, polarity index = 3.1) (AlSaeed et al., 2022; Micikas et al., 2022; Nguyen et al., 2023; Gu and Ma, 2023). Therefore, the DMF-DCM combination with a 1:3 ratio was chosen for subsequent studies. According to the results, the solvent's polarity and dielectric constant are crucial variables in determining the payload's adsorption and loading effectiveness.

3.4.2. Impact of CHT loading periods

Fig. 6 (A2 & B2) show the impact of adsorption durations on the percentage of CHT adsorption and loading, respectively. The process's equilibrium time was studied using various periods to ascertain the ideal AE and CHT loading time. The CHT-carrier ratio used to investigate the current assessment was constant at 1:3 (w/w) using the optimized DMF-DCM mixture ratio of 1:3 (v/v). It is evident that when the loading duration increased within 24 h, the CHT loading content and AE were significantly enhanced ($P < 0.05$). The CHT adsorption on the silica carriers had achieved equilibrium at 24 h, recording 21.97 % and 84.51 % for CHT loading and AE, respectively. As the loading duration was extended to 48 h, the CHT adsorption and loading content remained constant, revealing no significant change ($P > 0.05$) between 24 and 48 h. As a result, the best CHT adsorption time was 24 h.

3.4.3. Influence of CHT-nanocarrier mass ratios

In the current experiment, CHT adsorption procedures were performed in a DMF-DCM mixture at 1:3 (v/v) and continued for 24 h using several CHT/nanomaterials mass ratios to study the correlation between CHT loading capacity and CHT/carrier ratio (w/w). Fig. 6 (A3 & B3) show that the CHT AE rose significantly ($P < 0.05$) from 17.38 % to 82.22 % when the mass ratio of CHT to nanoparticles was reduced from 1:1 to 1:3 (w/w), while the AE remained stable at 83.28 % at 1:4 ratio, showing that drug adsorption had achieved equilibrium. However, when the mass of the nanoparticles grew, the CHT loading content improved statistically ($P < 0.05$) from 1:1 (14.8 %) to 1:3 (21.51 %) and subsequently decreased at a ratio of 1:4 (17.44 %) due to the larger mass of nanoparticles. Therefore, in order to proceed with further investigation, the ideal loading circumstances, which included a 24 h loading period, a DMF: DCM ratio of 1:3 (v/v), and CHT: NH_2_MSNPs at a ratio of 1:3 (w/w), were chosen. This resulted in an AE of 82 % and a loading efficiency of 21 %. For the purposes of comparison, CHT was loaded into the unmodified MSNPs under ideal circumstances, and the results indicated an AE of 53.95 % and a loading content of 15.24 %. However, non-functionalized silica has a greater surface area, pore volume, and diameter than functionalized silica; the aminopropyl grafted silica exhibits superiority in CHT loading and adsorption. This analysis shows that the modified NH_2_MSNPs have much more storage capacity than non-functionalized MSNPs. These findings proved that aminopropyl-functionalization plays a crucial role in CHT uptake (Berlier et al., 2013; Sapino et al., 2015).

3.5. TGA analysis

The quantity of aminopropyl functional groups, polymer content, and total CHT loading in the inclusion complexes were all determined by thermogravimetric analysis. Fig. 7 shows representative thermograms of the as-prepared samples. As reported before, comparing the materials' weight losses enabled us to determine the proportions of various functional groups, including CHT molecules (Berlier et al., 2013; Sapino et al., 2015). Two separate zones of weight reduction were seen in the unmodified MSNPs. The thermodesorption of physically adsorbed water molecules and loss of organic solvents are responsible for the first area of mass loss, which is 7.98 % and occurs in the temperature range between 25 and 100 °C. The weight loss in the second zone, where the temperature is between 100 and 800 °C, is relatively small (1.41 %) due to the silanol groups' condensation. Therefore, the pure silica matrix exhibited high levels of thermal stability over the tested temperature spectrum.

Table 2
Percentage of weight loss versus temperature of different MSNPs samples.

Samples	Percentage of weight loss (wt.%)		Total weight loss(wt. %)
	25–100 °C	100–800 °C	
MSNPs	7.98	1.41	9.39
NH_2_MSNPs	5.30	14.13	19.43
NH_2_MSNPs/CHT	5.63	33.94	39.57
NH_2_MSNPs/CHT@EUS-100	9.12	49.52	58.64

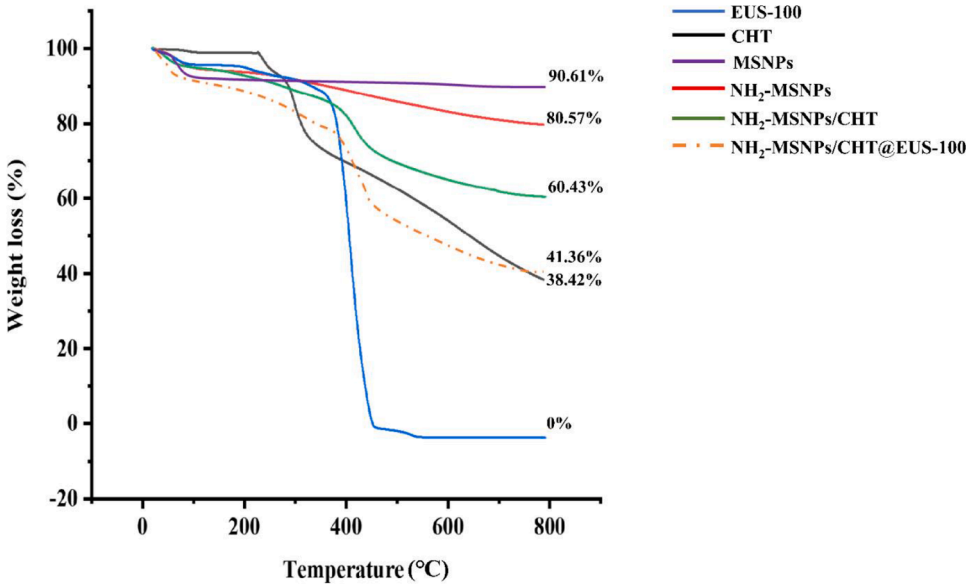

Fig. 7. TG analysis of the catechin, Eudragit®S-100, pristine silica, amino-modified silica, catechin-loaded, and polymer and coated NH_2_MSNPs. The measurements were done in a nitrogen atmosphere (10 mL/min) at a temperature rate of 10°C/min from 25 to 800°C.

Functionalized silica exhibits a significantly different thermogram compared to bare silica nanoparticles. The first zone revealed a decrease in weight by 5.30 % overall, while the second region had a 14.13 % weight drop. The functionalized nanocarrier exhibits a lower weight loss value in the primary area, likely due to less water adsorption, the materials being more hydrophobic, and a decline in its effective silanol concentration (de Oliveira Freitas et al., 2017). The weight loss between 100 and 800 °C indicates that the inserted organic material (aminopropyl group) is decomposing. The total weight loss of 9.39 % and 19.43 % for MSNPs and NH_2–MSNPs, respectively, confirm the anchoring of the aminopropyl group to the surface of silica nanoparticles by 12.72 wt %.

CHT demonstrated four phases of weight reduction, as seen in Fig. 7. The initial weight loss (1.9 %) was due to removing water between 30 and 150 °C, while further weight losses occurred at temperatures over 151 °C due to CHT breakdown. In particular, the mass of the CHT dropped by 5.22 % in the second stage (151–265 °C), 15.85 % in the third phase (266–330 °C), and 38.61 % in the final region (331–800 °C) (Liu et al., 2014). The NH_2–MSNPs/CHT materials' TG curves demonstrate CHT deterioration in nearly the same temperature range. It reveals that CHT is distributed differently, loaded within the functionalized carrier's channels, and physically adsorbed outside the pores, perhaps in the secondary mesopores between the nanoparticles. The findings imply that NH_2–MSNP carriers' pores may be loaded effectively. This phenomenon could be illustrated by the creation of hydrogen bonds between the hydroxyl groups of CHT and aminopropyl groups in the smaller pores of the modified nanomaterials, which can be obtained in excellent agreement with the FT-IR measurements. Following corrections for moisture and aminopropyl concentration, TG analysis was used to estimate the actual CHT content of the carriers. As shown in Fig. 7 and Table 2, the total weight loss jumped to 39.57 % (residual mass = 60.43 %) after CHT loading into the nanocarriers, indicating the success of CHT loading into the matrix of nanoparticles by 19.81 wt%. The results of the CHT loading by TGA study (19.81 wt%) are in good agreement with those obtained from the UV spectrophotometric readings (21.51 wt %).

The amount of polymer was determined by adjusting the measured weight loss for a given quantity of aminopropyl and CHT. Loss of CHT during coating was used to check the concentration of the loaded CHT to ensure accurate CHT amount subtraction. The anchoring of pH-sensitive polymer on the nanoparticle surface did not reduce the quantity of CHT present, as shown by the fact that it was equivalent to that found in non-coated samples. These findings were consistent with the previously reported results (Popova et al., 2018). The EUS-100 TGA scan showed a mass loss of 7 % up to 250 °C owing to the elimination of absorbed moisture. Still, thermal degradation was also indicated by a significant mass decrease (88 %) during the 251 to 450 °C temperature range (Gioumouxouzis et al., 2018). The weight drop of the coated nanoparticles was 58.64 % (residual mass = 41.36 %). The mass reduction of the nanoparticles due to the breakage of the EUS-100 layers was 19.07 % (Fig. 7, Table 2). The polymer-coated sample's TG curves exhibit a considerable and abrupt weight loss step above 350 °C, primarily due to the degradation of the produced EUS-100 layers. These results imply that the surface of pure MSNPs were efficiently modified with amino groups, resulting in NH_2–MSNPs carriers. Furthermore, the pores of these carriers were successfully loaded with CHT and eventually coated with EUS-100, which acts as a pH-sensitive gatekeeper.

3.6. DSC analysis

Knowing the physical state of the drug inside nanoparticles might be helpful since amorphous forms frequently have higher bioaccessibility than crystalline ones (Pool et al., 2017). Therefore, PXRD and DSC were employed to ascertain the structural integrity of the CHT embedded inside the silica nanospheres. Medications that are crystallized may be measured and identified using DSC by their prominent melting peaks. On the other hand, peaks may be absent if the payload is in an amorphous or noncrystalline condition (Biswas, 2017). Fig. 8 presents the DSC thermograms of pure CHT, EUS-100, MSNPs, NH_2–MSNPs, NH_2–MSNPs/CHT, and NH_2–MSNPs/CHT@EUS-100. The CHT DSC curves revealed various endothermic transitions at 121.09 °C and 137.86 °C, which are related to the dehydration of the attached moisture, 174.53 °C and 218.96 °C, which correspond to the melting temperature of CHT, emphasizing the crystallization of it, and at 293.18 °C, which are correlated to the degradation of the CHT (Pool et al., 2012; Dias et al., 2008; Dudhani and Kosaraju, 2010). The absence of any clear peaks in DSC curves of pure and aminated MSNPs is attributed to their amorphous nature. The DSC thermogram of the EUS-100 exhibited two distinct endothermic peaks, encompassing temperatures ranging from 80 to 135 °C and 227 to 257 °C, respectively. These peaks indicate the occurrence of the material's transition and melting processes (Zafar et al., 2023; Asfour and Mohsen, 2018; Parikh et al., 2016). The thermogram of the NH_2–MSNPs/CHT and NH_2–MSNPs/CHT@EUS-100 did not display the characteristic peaks of CHT, implying that CHT had

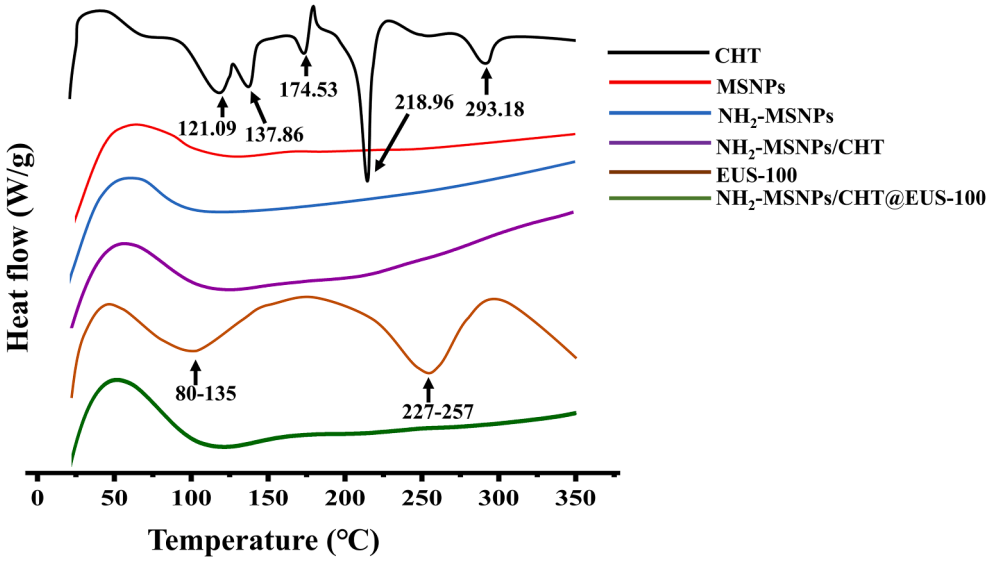

Fig. 8. DSC thermograms of catechin, Eudragit®S-100 various silica nanocarriers. Samples were heated from 25 to 350 °C at the rate of 10 °C/min in the presence of nitrogen at a flow rate of 50 mL/min.

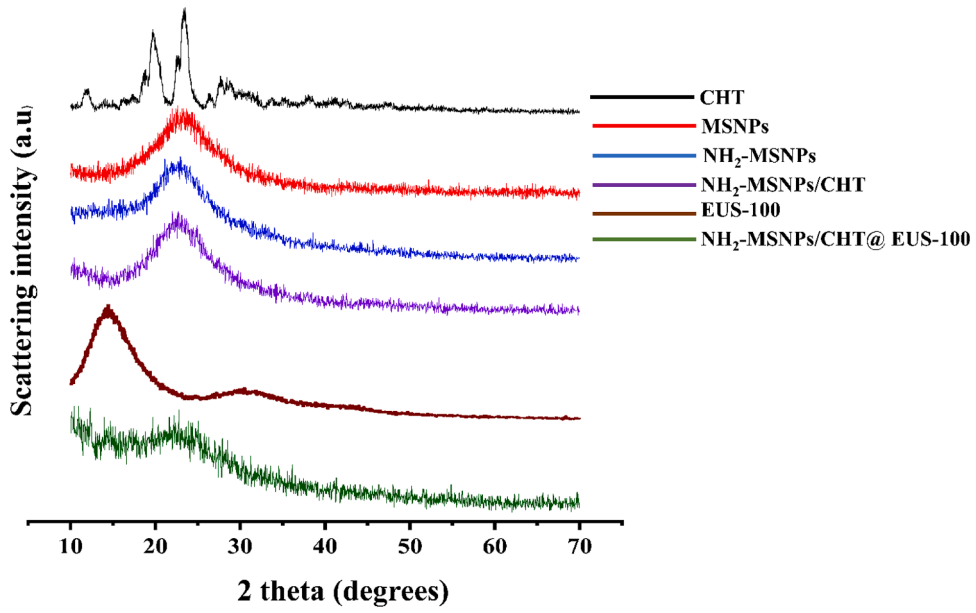

Fig. 9. PXRD pattern of catechin, Eudragit®S-100, and different silica nanoparticles. The angular scan was performed at a rate of 1°/min, ranging from 10° to 70° with a diffraction angle of 2-theta with a step size of 0.02 (4 s/step).

formed in an amorphous state (Salonen et al., 2005).

3.7. PXRD studies

The PXRD analysis confirmed that the fully loaded CHT experienced a transformation into an amorphous state. The loading of medication into mesopores of silica nanoparticles is known to convert their crystalline into an amorphous nature and hinder recrystallization (Juère et al., 2017). Pure CHT's Diffraction patterns display multiple peaks in the 10° to 30° range at 11.96°, 18.64°, 19.67°, 22.47°, 23.47°, 26.34°, and 28.88° (2θ) angles, which correspond to different lattice orientations in the crystalline molecule (Fig. 9). These observations were in good agreement with the results described by Sinsinwar and Vadivel (2021) and Sinsinwar and Vadivel (2021). The lack of distinct crystalline peaks in the measured 2-theta range demonstrates the amorphous nature of pure and modified silica nanoparticles. The CHT-loaded aminated nanoparticles exhibited no diffraction signal corresponding to pure CHT, referring to a transition of the loaded CHT molecules from a crystalline to an amorphous form. The amorphous nature of EUS-100 was confirmed by the presence of two broad diffraction peaks at 2θ =

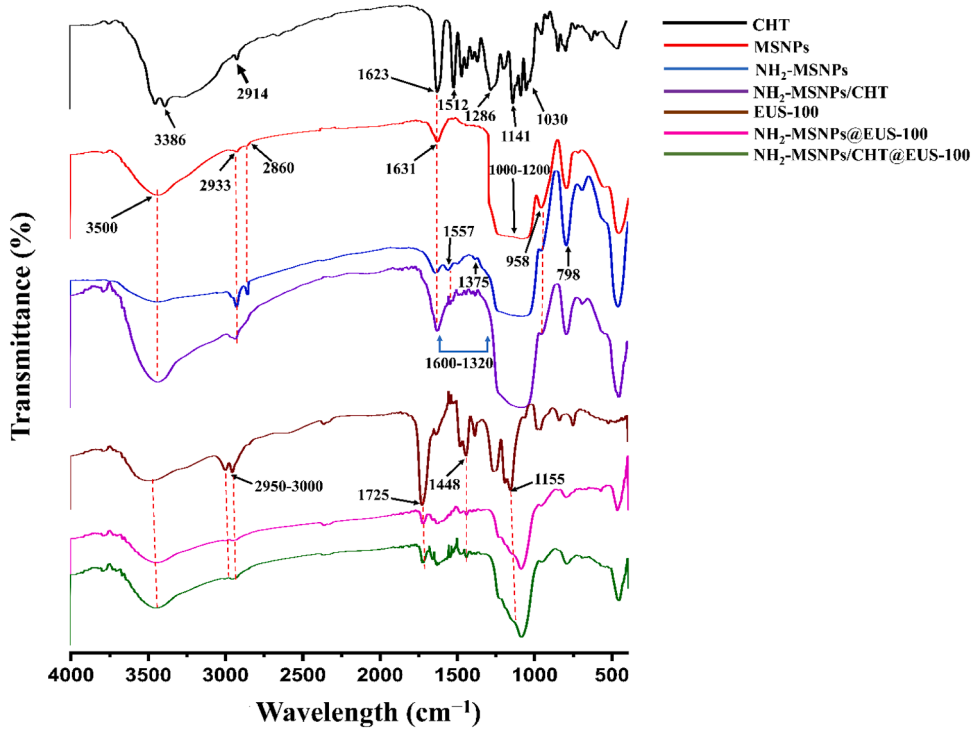

Fig. 10. FT-IR spectra for catechin, Eudragit®S-100, bare MSNPs, NH_2–MSNPs, loaded NH_2–MSNPs, NH_2–MSNPs@EUS-100, and NH_2–MSNPs/CHT@EUS-100. One hundred scans were collected for each FT-IR over the wavenumber region 4000–400 cm^{-1} 1at 4 cm^{-1} resolution.

14.73° and 31.52° (Sunoqrot and Abujamous, 2019). It seems that the loaded CHT is confined inside the NH_2_MSNPs and polymer nanocomposites in an amorphous state since no diffraction peaks resulting from crystalline CHT were identified for the CHT-loaded nanoparticles with EUS-100 coating. Thus, it could be concluded that it is probable that the CHT and the whole system in NH_2_MSNPs/CHT@EUS-100 nanocarrier are still entirely amorphous.

3.8. FT-IR spectroscopy

FT-IR analysis was used to determine the chemical reaction between nanocarriers and the drug, detect changes in bonds of the guest and host molecules, vibrational modes disruption, and assess the chemo-functional groups found in the structure of the active ingredient (Li et al., 2019). The active agent of the current study's FT-IR peak's form, intensity, and location is somewhat different from the silica materials, which suggests encapsulation. Fig. 10 displays the FT-IR spectra of CHT, MSNPs, NH_2_MSNPs, NH_2_MSNPs/CHT, EUS-100, NH_2_MSNPs@EUS-100 and NH_2_MSNPs/CHT@EUS-100. FT-IR spectra of CHT revealed a distinctive relatively sharp peak of OH stretch of the phenolic hydroxyl groups connected to the aromatic rings at 3386.05 $cm^{-1,}$ and CHT's apparent band at 2914.91 cm^{-1} may be due to C–H stretching (Sinsinwar and Vadivel, 2021; Selestin Raja et al., 2018). Additionally, the C–H (methylene) group may be identified by a peak at 1512.31 cm^{-1}. Bands at 1623.83 and 1141.18 cm^{-1} in the IR spectrum of CHT represent aromatic C–C stretching and aromatic C=C stretching in-plane distortion. CHT has a strong C–O stretching band at 1030.36 cm^{-1} and a prominent peak at 1286.45 cm^{-1}, related to the C–O aromatic ester group.

A wide band (1200–1000 cm^{-1}) was seen in the bare MSNPs spectra, which corresponded to the asymmetric vibration of the group (Si–O–Si). In addition, the vibrational asymmetry of Si–OH and the vibrational symmetry of Si–O are responsible for the bands seen at 958.96 cm^{-1} and 798.90 cm^{-1}, respectively. The appearance of a band at 1631.19 cm^{-1} caused by molecular water's scissor bending and the presence of a highly distinctive absorption band at 3500 cm^{-1} was shown by O–H stretching in H–bonded water. Furthermore, the presence of traces of unreacted TEOS is what is responsible for the little bands at 2933.67 cm^{-1} (CH_3) and 2860.73 cm^{-1} (CH_2) (Beganskiene et al., 2004; Arriagada et al., 2016). Regarding the NH_2_MSNPs spectrum, which shows some changes when compared with the pure MSNPs FT-IR, the band at 3500 cm^{-1}, which corresponds to O–H stretching of molecular water, and the band centered at 958.96 cm^{-1} and is related to asymmetric vibration of Si–OH reduced in intensity. A new band at 1375.1 cm^{-1}, corresponding to the Si–CH_2 bending mode, emerged, implying the existence of the NH_2 group of the APTES molecule attached to the terminal part of the propyl chain. An additional signal attributed to NH_2 asymmetric bending was seen at 1557.31 cm^{-1}, beside the bands at 2933.67 cm^{-1} and 2860.73 cm^{-1} that slightly expanded owing to the vibration of the (CH_2) group of the propyl chain. This suggests that the surface's concentration of Si–OH groups have dropped, and its concentration of NH_2 groups has grown, indicating effective APTES grafting (Kamiya et al., 2000; Rahman et al., 2009).

No novel peaks appeared in the loaded NH_2_MSNPs/CHT spectra, suggesting no chemical interactions occurred between CHT and pure MSNPs. CHT molecules exhibited hydrogen bonding with silanol groups on the silica surface as a consequence of shifting in the loaded MSNPs and weakening of the characteristic peaks of CHT. In particular, The IR spectrum of the loaded NH_2-nanocarrier showed at least three significant differences in comparison with MSNPs and modified MSNPs spectra. First, some changes were observed in the 1320–1600 cm^{-1} region due to the bands' superposition and shift corresponding to the CHT aromatic ring's C–C skeletal vibration. Second, the band ascribed to the NH_2 asymmetric bending (1557.31 cm^{-1}) diminished considerably; these findings suggest that CHT was successfully incorporated into silica nanoparticles through the interaction with the amino group of APTES. Finally, the CHT–OH groups on the surface of the nanoparticles caused the bands orientated at 3500 cm^{-1} to become more intense, a finding in accordance with other authors (Arriagada et al., 2016; Vickers, 2017). The utilized ratio and interaction with NH_2_MSNPs during loading may be connected to the pronounced presence of NH_2_MSNPs in the spectrum, the weakening of the CHT's distinctive peaks, and the hiding of other and, therefore, bands. The spectra were analyzed in great detail, and the results confirmed the presence and integrity of CHT molecules inside the silica pores; the NH_2 group of APTES and the OH group of CHT are involved in the interaction between nanoparticles and CHT, and the preservation of the CHT's pharmacophore.

The C–O stretching, C–H bending, C=O stretching, and C–H stretching bands in the FT-IR spectra of EUS-100 were identified at 1155.05 cm^{-1}, 1448.15 cm^{-1}, 1725.32 cm^{-1}, and 2950–3000 cm^{-1}, respectively (Borderwala et al., 2021; Pritam et al., 2022). The characteristic peak of EUS-100 at 1155.05 cm^{-1}, in NH_2_MSNPs@EUS-100, overlaps the band of pure silica nanoparticles in the region of 1200–1000 cm^{-1}, and the form of the combined peak is quite reminiscent of the shape of the characteristic peak of a polymer that is close to the surface. If faintly, EUS-100′s signature bands are easily visible in NH_2_MSNPs@EUS-100 samples, proving that the coating of EUS-100 to the aminated particles was effective. The NH_2_MSNPs/CHT@EUS-100 exhibited no unexpected peaks in their spectra, confirming the absence of a chemical interaction or modification to the pharmacophore CHT.

3.9. Release of CHT from silica nanoparticles

The capacity of the delivery method to shield the cargo from the GIT environment until it reaches the colon, at which the pH will promote drug release by encouraging polymer breakdown, is necessary for effective colon targeting using pH-sensitive nanoparticles. By performing a release test in a medium with different pH values, we confirmed that CHT-loaded NH_2_MSNPs/CHT@EUS-100 may successfully accomplish this aim. Drug-loaded nanoparticles were suspended in aqueous buffer solutions (USP universal buffer, pH 1.9) to examine pH-responsive in vitro release. To mimic the progressive elevation of gastrointestinal tract (GIT) pH, the buffer pH shifted from 5.5 to 7.4 at 2 and 5 h intervals (Castangia et al., 2015) (Qu et al., 2021). The in vitro release profiles of free CHT and several formulations of CHT produced in a USP universal buffer are shown in Fig. 11.

At a pH of 1.9, non-encapsulated CHT rapidly releases approximately 95 % in the first 2 h. Therefore, one would anticipate that the non-encapsulated flavonoid would undergo fast oxidative and metabolic degradation in the GIT-simulating conditions, decreasing its biological function. After 3 h, almost all loaded CHT was released without any indication of drug precipitation during the next 24 h. About 79 % of CHT was released from MSNPs/CHT during the first 2 h. However, NH_2_MSNPs/CHT showed only 52 % CHT release in the first 2 h (pH 1.9). This may be explained by the aminated material having a smaller pore size and volume than pristine nanoparticles and by developing a hydrogen bond between the CHT and NH_2 of the aminopropyl chain. The cumulative percentage of CHT released after 24 h was approximately 100 % and 90 % for MSNPs/CHT and NH_2_MSNPs/CHT, respectively. MSNPs/CHT and NH_2_MSNPs/CHT formulations have two-step CHT release properties. Due to the presence of CHT being close to the pore surface and CHT being connected to the surface, the burst release pattern attained in the first stage may have been possible. The last phase showed the establishment of the slow sustained release profile, which may have been brought on by CHT being deeply adsorbed in the silica pores. Kinetic release modelling supported these results, demonstrating that the CHT dissolution rate from the pure and decorated MSNPs was diffusion-regulated.

CHT release from EUS-100 coated NH_2_MSNPs/CHT has been verified to be pH-responsive, with less than 2 % being released at pH 1.9 and an additional 4 % being released at pH 5.5; when the pH was raised to 7.4, around 90 % of the CHT was released in the colonic pH. Only 6 % of

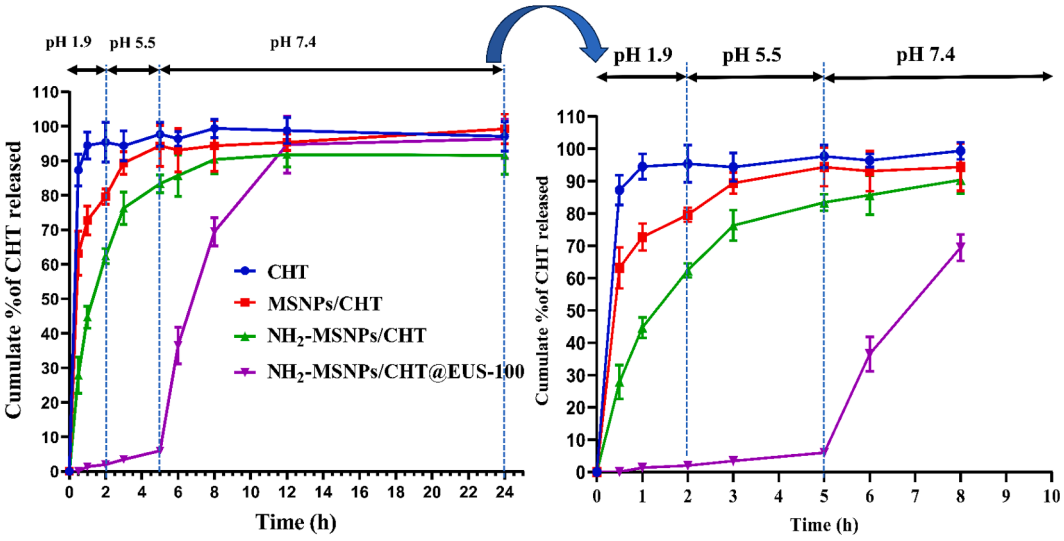

Fig. 11. In vitro release profiles of pure catechin, MSNPs/CHT, NH_2_MSNPs/CHT, and NH_2_MSNPs/CHT@EUS-100 in universal buffers at 37 ± 0.5 °C and 100 rpm. The release was started at pH 1.9 for the first 2 h. Then, the pH was adjusted to 5.5 for 3 h. At last, pH was adjusted to 7.4 till the end of the release. Data represent mean ± SD, (n = 3).

Table 3
Release Kinetics of CHT from MSNPs/CHT, NH_2_MSNPs/CHT and NH_2_MSNPs/CHT@EUS-100 using different kinetic models.

Formula	Zero-order R^2	First- order R^2	Hixon-Crowell R^2	Higuchi- order R^2	Korsmeyer-Peppas R^2	Korsmeyer-Peppas *n*	Release order	Main release mechanism
MSNPs/CHT	0.6955	0.9435	0.8648	0.8388	**0.9844**	0.2662	Korsmeyer-Peppas	Fickian diffusion
NH_2_MSNPs/CHT	0.6579	0.7745	0.7377	0.8162	**0.9146**	0.3073	Korsmeyer-Peppas	Fickian diffusion
NH_2-SNPs/CHT@EUS-100	0.8745	0.9244	0.9118	0.9088	**0.9937**	1.886	Korsmeyer-Peppas	supercase II transport

the CHT was released from NH_2_MSNPs/CHT@EUS-100 owing to leaching in the dissolving medium of pH 1.2 and pH 4.5, which was adequate to produce a lag period of about 5 h in GIT since EUS-100 is soluble more readily at pH > 7. These results demonstrate that CHT may be shielded from stomach acidity and throughout intestinal transit by coated nanocarrier with the enteric coated polymer (EUS-100). This is due to EUS-100′s methacrylic acid moieties being protonated at low pH and covering the loaded CHT, rendering them insoluble and hindering CHT release. Electrostatic repulsion and polymer swelling brought about by the enhanced ionization of the methacrylic acid moieties in the polymer at pH above 7 resulted in opening the pH-responsive gate and releasing the encapsulated CHT. Our findings are in line with the results seen in prior studies (Raza et al., 2021; Kumeria et al., 2020; Sunoqrot and Abujamous, 2019). This data confirms the use of NH_2_MSNPs/CHT@EUS-100 nanosystem for colon-specific administration. Overall, the in vitro drug release investigation showed that CHT-loaded NH_2_MSNPs coated with EUS-100 enabled pH-responsive controlled release at a simulated colonic pH and prevented CHT from being released too early in the low pH medium.

3.10. Mechanism of CHT release from various silica nanosystems

Fitting experimental data of CHT release with Eqs. (3-7) determined the CHT releasing mechanism. Table 3 displays the estimated results for all reported CHT kinetic models. According to the best fit with the highest coefficient of correlation (R^2) value, all tested formulations follow the Korsmeyer-Peppas model with varying release exponent values. In the case of MSNPs/CHT and NH_2_MSNPs/CHT, the Fickian diffusion process was assumed since the release exponent (*n*) values were less than 0.45. It is possible that CHT molecules leached from the nanoparticle pores, causing the immediate release, resulting in the CHT diffusing from the system's channels. Values of $n > 0.85$ for NH_2_MSNPs/CHT@EUS-100 imply supercase II transport, in which CHT release is driven solely by polymer relaxation (Siepmann and Peppas, 2012; de Oliveira Freitas et al., 2017; Sunoqrot et al., 2022). According to Table 3, the release data showed an excellent match (R^2 = 0.9937) with the Korsmeyer-Peppas model, with an *n* value of 1.886, demonstrating that CHT release was mainly regulated by the swelling-relaxation process of the polymer chain upon ionization of the methacrylate moieties when subjected to a neutral pH condition.

3.11. Stability studies

The findings from the stability investigation are shown in Table 4. The stability analysis of NH_2_MSNPs/CHT@EUS-100 revealed no statistically significant differences ($P > 0.05$)s in all the characterizations before and after a storage period of 3 months. The particle size was maintained below 200 nm and exhibited a favourable size distribution of

Table 4
Results of stability studies for the NH_2_MSNPs/CHT@EUS-100 Nanoparticles. The studies were done at a temperature 25°C and a relative humidity of 75%.

Characterization	Initial (zero time)	After 1 month	After 2 months	After 3 months
Particle size (nm)	159.67 ± 8.24	151.48 ± 6.69	155.37 ± 5.29	158.38 ± 9.45
PDI	0.23 ± 0.09	0.26 ± 0.06	0.19 ± 0.08	0.27 ± 0.04
Zeta potential (mV)	−40.25 ± 4.46	−36.05 ± 6.34	−39.14 ± 6.76	−42.18 ± 3.49
CHT AE (%)	80.49 ± 5.67	77.20 ± 3.42	82.06 ± 2.31	79.69 ± 4.50

less than 0.3. Furthermore, it was noted that the zeta potential showed no changes and stayed constant at around −40 mV during the storage period. This indicates that there were no chemical alterations on the surfaces of the particles and that they demonstrated adequate stability. It could be concluded that the synthesized silica nanoparticles exhibit an impressive degree of stability and effectively protect the enclosed medication from environmental influences. Furthermore, it was observed that applying a coated film of EUS-100 seemed to operate as a gatekeeper, effectively inhibiting the leakage of the medication from the mesopores of silica nanoparticles.

4. Conclusion

It is crucial to design innovative oral formulations and discover creative ways to construct efficient therapeutic systems of colon targeting. To our knowledge, this is the first research to create and optimize a colon targeting oral CHT formulations based on pH-responsive mesoporous silica nanosystems. The amine terminals were successfully grafted by the post-synthesis method onto the surface of effectively developed pristine silica nanoparticles, making them an ideal host for the visiting guest (the PH-responsive polymer, EUS-100) and improving the loading content of CHT. It has been demonstrated that many parameters affect NH_2_MSNPs' capacity to load CHT, particularly the polarity index of solvent, CHT adsorption period, and CHT-carrier mass ratio, decreasing the solvent's polarity parameter or boosting the CHT-to-carrier mass ratio could improve the CHT adsorption markedly. The polymer coating of the modified silica samples with EUS-100 shielded the loaded CHT from the acidic environment of the GIT before reaching the colonic site and inhibited the premature release of CHT. Overall, mesoporous silica nanoparticles coated with the pH-responsive polymer show promise as a novel, affordable oral delivery strategy for colon targeting therapy. Our future studies will examine the in vivo pharmacokinetics of the CHT released and define how particle uptake (qualitative and quantitative) affects disease pathology, both with and without a pH-responsive coating.

Funding

This research was funded by Princess Nourah bint Abdulrahman University Researchers Supporting Project number (PNURSP2023R166), Princess Nourah bint Abdulrahman University, Riyadh, Saudi Arabia.

CRediT authorship contribution statement

Abdulsalam M. Kassem: Conceptualization, Methodology, Formal analysis, Project administration. **May Almukainzi:** Writing – review & editing. **Tarek M. Faris:** Resources, Validation. **Ahmed H. Ibrahim:** Investigation, Methodology. **Walid Anwar:** Software. **Ibrahim A. Elbahwy:** Investigation. **Farid R. El-Gamal:** Data curation, Writing – original draft. **Mohamed F. Zidan:** Investigation. **Mohamed A. Akl:** Data curation, Writing – original draft. **Ahmed M. Abd-ElGawad:** Visualization. **Abdelsamed I. Elshamy:** Data curation, Methodology. **Mohammed Elmowafy:** Supervision, Writing – review & editing.

Declaration of Competing Interest

The authors declare that they have no conflicts of interest.

Data availability

Data will be made available on request.

References

Ahmad, N., Ahmad, R., Alrasheed, R.A., Almatar, H.M.A., Al-Ramadan, A.S., Amir, M., Sarafroz, M., 2020. Quantification and evaluations of catechin hydrate polymeric nanoparticles used in brain targeting for the treatment of epilepsy. Pharmaceutics 12, 203.

Alali, M., Alqubaisy, M., Aljaafari, M.N., Alali, A.O., Baqais, L., Molouki, A., Abushelaibi, A., Lai, K.S., Lim, S.H.E., 2021. Nutraceuticals: transformation of conventional foods into health promoters/disease preventers and safety considerations. Molecules 26. https://doi.org/10.3390/molecules26092540.

AlSaeed, H., Amin, M.O., Al-Hetlani, E., 2022. Forensic analysis of cosmetic smudges using surface-assisted laser desorption/ionization mass spectrometry: recovery and ageing study. Microchem. J. 180, 107609.

Arriagada, F., Correa, O., Günther, G., Nonell, S., Mura, F., Olea-Azar, C., Morales, J., 2016. Morin flavonoid adsorbed on mesoporous silica, a novel antioxidant nanomaterial. PLoS One 11, e0164507.

Asfour, M.H., Mohsen, A.M., 2018. Formulation and evaluation of pH-sensitive rutin nanospheres against colon carcinoma using HCT-116 cell line. J. Adv. Res. 9, 17–26.

Athirojthanakij, W., Rashidinejad, A., 2023. Delivery of catechins from green tea waste in single-and double-layer liposomes via their incorporation into a functional green kiwifruit juice. Molecules 28, 575.

Awad, A., Madla, C.M., McCoubrey, L.E., Ferraro, F., Gavins, F.K.H., Buanz, A., Gaisford, S., Orlu, M., Siepmann, F., Siepmann, J., others, 2022. Clinical translation of advanced colonic drug delivery technologies. Adv. Drug Deliv. Rev. 181, 114076.

Badihi, R., Mahmoudi, A., Sazegar, M.R., Nazari, K., 2022. A study on co-modification of MSNs with some transition metals and polyethyleneimine (PEI) as a versatile strategy for efficient delivery of short oligonucleotides. Chem. Pap. 76, 7023–7035.

Beganskiene, A., Sirutkaitis, V., Kurtinaitien\.e, M.., Juš k\.enas, R., Kareiva, A., 2004. FTIR, TEM and NMR investigations of Stöber silica nanoparticles. Mater Sci 10, 287–290.

Berlier, G., Gastaldi, L., Sapino, S., Miletto, I., Bottinelli, E., Chirio, D., Ugazio, E., 2013. MCM-41 as a useful vector for rutin topical formulations: synthesis, characterization and testing. Int. J. Pharm. 457, 177–186.

Biswas, N., 2017. Modified mesoporous silica nanoparticles for enhancing oral bioavailability and antihypertensive activity of poorly water soluble valsartan. Eur. J. Pharm. Sci. 99, 152–160.

Blanco-Llamero, C., Fonseca, J., Durazzo, A., Lucarini, M., Santini, A., Señoráns, F.J., Souto, E.B., 2022. Nutraceuticals and food-grade lipid nanoparticles: from natural sources to a circular bioeconomy approach. Foods 11, 2318.

Borderwala, K., Rathod, S., Yadav, S., Vyas, B., Shah, P., 2021. Eudragit S-100 surface engineered nanostructured lipid carriers for colon targeting of 5-fluorouracil: optimization and in vitro and in vivo characterization. AAPS PharmSciTech 22, 216.

Cai, X., Wang, X., He, M., Wang, Y., Lan, M., Zhao, Y., Gao, F., 2021. Colon-targeted delivery of tacrolimus using pH-responsive polymeric nanoparticles for murine colitis therapy. Int. J. Pharm. 606, 120836.

Castangia, I., Nácher, A., Caddeo, C., Merino, V., Díez-Sales, O., Catalán-Latorre, A., Fernàndez-Busquets, X., Fadda, A.M., Manconi, M., 2015. Therapeutic efficacy of quercetin enzyme-responsive nanovesicles for the treatment of experimental colitis in rats. Acta Biomater. 13, 216–227. https://doi.org/10.1016/j.actbio.2014.11.017.

Chen, J., Lu, W.L., Gu, W., Lu, S.S., Chen, Z.P., Cai, B.C., Yang, X.X., 2014. Drug-in-cyclodextrin-in-liposomes: a promising delivery system for hydrophobic drugs. Expert Opin. Drug Deliv. 11, 565–577.

Chourasiya, V., Bohrey, S., Pandey, A., 2016. Formulation, optimization, characterization and in-vitro drug release kinetics of atenolol loaded PLGA nanoparticles using 33 factorial design for oral delivery. Mater. Discov. 5, 1–13.

Contreras, C.B., Azzaroni, O., Soler-Illia, G., 2019. 1.16 Use of confinement effects in mesoporous materials to build tailored nanoarchitectures. Compr. Nanosci. Nanotechnol. 2, 331–348.

da Fonseca Machado, A.P., Arruda, H.S., Reguengo, L.M., de Moura, L.D., de Carvalho, F. V., do Nascimento, R., de, P., Junior, M.R.M., 2023. Encapsulating products. Natural Plant Products in Inflammatory Bowel Diseases. Elsevier, pp. 319–364.

de Oliveira Freitas, L.B., de Melo Corgosinho, L., Faria, J.A.Q.A., dos Santos, V.M., Resende, J.M., Leal, A.S., Gomes, D.A., de Sousa, E.M.B., 2017. Multifunctional mesoporous silica nanoparticles for cancer-targeted, controlled drug delivery and imaging. Microporous Mesoporous Mater. 242, 271–283.

Dias, K., Nikolaou, S., De Giovani, W.F., 2008. Synthesis and spectral investigation of Al (III) catechin/β-cyclodextrin and Al (III) quercetin/β-cyclodextrin inclusion compounds. Spectrochim. Acta Part A Mol. Biomol. Spectrosc. 70, 154–161.

Dima, C., Assadpour, E., Dima, S., Jafari, S.M., 2020. Bioavailability of nutraceuticals: role of the food matrix, processing conditions, the gastrointestinal tract, and nanodelivery systems. Compr. Rev. food Sci. food Saf. 19, 954–994.

Ditu, L.M., Grigore, M.E., Camen-Comanescu, P., Holban, A.M., 2018. Introduction in nutraceutical and medicinal foods. Therapeutic, Probiotic, and Unconventional Foods. Elsevier, pp. 1–12.

Dubey, R.S., Rajesh, Y., More, M.A., 2015. Synthesis and characterization of SiO2 nanoparticles via sol-gel method for industrial applications. Mater. Today Proc. 2, 3575–3579.

Dudhani, A.R., Kosaraju, S.L., 2010. Bioadhesive chitosan nanoparticles: preparation and characterization. Carbohydr. Polym. 81, 243–251.

Dutta, P., Mukherjee, K., Saha, A., Das, A., Badwaik, H.R., Giri, T.K., 2022. Colonic delivery of surface charge decorated nanocarrier for IBD therapy. J. Drug Deliv. Sci. Technol., 103754

Elmowafy, M., Alruwaili, N.K., Ahmad, N., Kassem, A.M., Ibrahim, M.F., 2023. Quercetin-loaded mesoporous silica nanoparticle–based lyophilized tablets for enhanced physicochemical features and dissolution rate: formulation, optimization,

and in vitro evaluation. AAPS PharmSciTech 24. https://doi.org/10.1208/s12249-022-02464-w.
Feng, W., Nie, W., He, C., Zhou, X., Chen, L., Qiu, K., Wang, W., Yin, Z., 2014. Effect of pH-responsive alginate/chitosan multilayers coating on delivery efficiency, cellular uptake and biodistribution of mesoporous silica nanoparticles based nanocarriers. ACS Appl. Mater. Interfaces 6, 8447–8460. https://doi.org/10.1021/am501337s.
Foppoli, A., Maroni, A., Moutaharrik, S., Melocchi, A., Zema, L., Palugan, L., Cerea, M., Gazzaniga, A., 2019. In vitro and human pharmacoscintigraphic evaluation of an oral 5-ASA delivery system for colonic release. Int. J. Pharm. 572, 118723.
Gioumouxouzis, C.I., Chatzitaki, A.T., Karavasili, C., Katsamenis, O.L., Tzetzis, D., Mystiridou, E., Bouropoulos, N., Fatouros, D.G., 2018. Controlled release of 5-fluorouracil from alginate beads encapsulated in 3D printed pH-responsive solid dosage forms. Aaps Pharmscitech 19, 3362–3375.
Gu, N., Ma, H., 2023. Study on ESIPT of salicylaldehyde derivative EQCN in DCM solvent. Spectrochim. Acta Part A Mol. Biomol. Spectrosc., 122968
He, K., Yang, J., Shi, Q., Guan, L., Sun, L., Chen, Z., Feng, J., Dong, S., 2022. Fluorescent aptamer-modified mesoporous silica nanoparticles for quantitative acetamiprid detection. Environ. Sci. Pollut. Res. 29, 88182–88192.
Ho, S., Thoo, Y.Y., Young, D.J., Siow, L.F., 2017. Cyclodextrin encapsulated catechin: effect of pH, relative humidity and various food models on antioxidant stability. LWT-Food Sci. Technol. 85, 232–239.
Hu, H., Yong, H., Yao, X., Yun, D., Huang, J., Liu, J., 2021. Highly efficient synthesis and characterization of starch aldehyde-catechin conjugate with potent antioxidant activity. Int. J. Biol. Macromol. 173, 13–25.
Ibrahim, A.H., Smått, J.H., Govardhanam, N.P., Ibrahim, H.M., Ismael, H.R., Afouna, M. I., Samy, A.M., Rosenholm, J.M., 2020. Formulation and optimization of drug-loaded mesoporous silica nanoparticle-based tablets to improve the dissolution rate of the poorly water-soluble drug silymarin. Eur. J. Pharm. Sci. 142, 105103 https://doi.org/10.1016/j.ejps.2019.105103.
Iraji, S., Ganji, F., Rashidi, L., 2018. Surface modified mesoporous silica nanoparticles as sustained-release gallic acid nano-carriers. J. Drug Deliv. Sci. Technol. 47, 468–476.
Janrao, C., Khopade, S., Bavaskar, A., Sudhakar Gomte, S., Agnihotri, T.G., Jain, A., 2022. Recent advances of polymer based nanosystems in cancer management. J. Biomater. Sci. Polym. Ed. 1–73.
Jena, A.B., Samal, R.R., Bhol, N.K., Duttaroy, A.K., 2023. Cellular Red-Ox system in health and disease: the latest update. Biomed. Pharmacother. 162, 114606.
Jia, X., Sheng, W., Li, W., Tong, Y., Liu, Z., Zhou, F., 2014. Adhesive polydopamine coated avermectin microcapsules for prolonging foliar pesticide retention. ACS Appl. Mater. Interfaces 6, 19552–19558.
Joudeh, N., Linke, D., 2022. Nanoparticle classification, physicochemical properties, characterization, and applications: a comprehensive review for biologists. J. Nanobiotechnology 20, 262.
Juère, E., Florek, J., Bouchoucha, M., Jambhrunkar, S., Wong, K.Y., Popat, A., Kleitz, F., 2017. In vitro dissolution, cellular membrane permeability, and anti-inflammatory response of resveratrol-encapsulated mesoporous silica nanoparticles. Mol. Pharm. 14, 4431–4441.
Kalhori, P., Abbasi, A., Malayeri, M.R., Shirazi, M.M., 2022. Impact of crude oil components on acid sludge formation during well acidizing. J. Pet. Sci. Eng., 110698
Kamarudin, N.H.N., Jalil, A.A., Triwahyono, S., Salleh, N.F.M., Karim, A.H., Mukti, R.R., Hameed, B.H., Ahmad, A., 2013. Role of 3-aminopropyltriethoxysilane in the preparation of mesoporous silica nanoparticles for ibuprofen delivery: Effect on physicochemical properties. Microporous Mesoporous Mater. 180, 235–241.
Kamiya, H., Mitsui, M., Takano, H., Miyazawa, S., 2000. Influence of particle diameter on surface silanol structure, hydration forces, and aggregation behavior of alkoxide-derived silica particles. J. Am. Ceram. Soc. 83, 287–293.
Kankala, R.K., Han, Y.H., Na, J., Lee, C.H., Sun, Z., Wang, S.B., Kimura, T., Ok, Y.S., Yamauchi, Y., Chen, A.Z., others, 2020. Nanoarchitectured structure and surface biofunctionality of mesoporous silica nanoparticles. Adv. Mater. 32, 1907035.
Kaur, R., Rajput, R., Nag, P., Kumar, S., Singh, M., 2017. Synthesis, characterization and evaluation of antioxidant properties of catechin hydrate nanoparticles. J. Drug Deliv. Sci. Technol. 39, 398–407. https://doi.org/10.1016/j.jddst.2017.04.030.
Kim, E.S., Lee, J.S., Lee, H.G., 2016. Calcium-alginate microparticles for sustained release of catechin prepared via an emulsion gelation technique. Food Sci. Biotechnol. 25, 1337–1343.
Krishnaiah, Y.S.R., Satyanarayana, V., Dinesh Kumar, B., Karthikeyan, R.S., Bhaskar, P., 2002. In vivo evaluation of guargum-based colon-targeted oral drug delivery systems of celecoxib in human volunteers. Eur. J. Drug Metab. Pharmacokinet. 27, 273–280.
Kumeria, T., Wang, J., Kim, B., Park, J.H., Zuidema, J.M., Klempner, M., Cavacini, L., Wang, Y., Sailor, M.J., 2020. Enteric polymer-coated porous silicon nanoparticles for site-specific oral delivery of IgA antibody. ACS Biomater. Sci. \& Eng. 8, 4140–4152.
Le Guével, X., Wegner, K.D., Würth, C., Baulin, V.A., Musnier, B., Josserand, V., Resch-Genger, U., Coll, J., 2022. Tailoring the SWIR emission of gold nanoclusters by surface ligand rigidification and their application in 3D bioimaging. Chem. Commun. 58, 2967–2970.
Li, C.F., Li, Y.C., Chen, L.B., Wang, Y., Sun, L.B., 2016. Doxorubicin-loaded Eudragit-coated chitosan nanoparticles in the treatment of colon cancers. J. Nanosci. Nanotechnol. 16, 6773–6780.
Li, W., Ran, L., Liu, F., Hou, R., Zhao, W., Li, Y., Wang, C., Dong, J., 2019. Preparation and characterisation of polyphenol-HP-β-cyclodextrin inclusion complex that protects lamb tripe protein against oxidation. Molecules 24, 4487.
Lin, M., Blevins, M.S., Sans, M., Brodbelt, J.S., Eberlin, L.S., 2022. Deeper understanding of solvent-based ambient ionization mass spectrometry: are molecular profiles primarily dictated by extraction mechanisms? Anal. Chem. 94, 14734–14744.
Liu, J., Lu, J., Kan, J., Wen, X., Jin, C., 2014. Synthesis, characterization and in vitro anti-diabetic activity of catechin grafted inulin. Int. J. Biol. Macromol. 64, 76–83.
Liu, R., Liao, P., Liu, J., Feng, P., 2011. Responsive polymer-coated mesoporous silica as a pH-sensitive nanocarrier for controlled release. Langmuir 27, 3095–3099.
Lv, J.M., Ismail, B.B., Ye, X.Q., Zhang, X.Y., Gu, Y., Chen, J.C., 2023. Ultrasonic-assisted nanoencapsulation of kiwi leaves proanthocyanidins in liposome delivery system for enhanced biostability and bioavailability. Food Chem 416, 135794.
Lv, X., Zhang, L., Xing, F., Lin, H., 2016. Controlled synthesis of monodispersed mesoporous silica nanoparticles: particle size tuning and formation mechanism investigation. Microporous Mesoporous Mater. 225, 238–244.
Mandel, S., Youdim, M.B.H., 2004. Catechin polyphenols: neurodegeneration and neuroprotection in neurodegenerative diseases. Free Radic. Biol. Med. 37, 304–317.
McCoubrey, L.E., Favaron, A., Awad, A., Orlu, M., Gaisford, S., Basit, A.W., 2023. Colonic drug delivery: formulating the next generation of colon-targeted therapeutics. J. Control. Release 353, 1107–1126. https://doi.org/10.1016/j.jconrel.2022.12.029.
Mei, X., Chen, D., Li, N., Xu, Q., Ge, J., Li, H., Lu, J., 2012. Hollow mesoporous silica nanoparticles conjugated with pH-sensitive amphiphilic diblock polymer for controlled drug release. Microporous Mesoporous Mater. 152, 16–24.
Melocchi, A., Uboldi, M., Briatico-Vangosa, F., Moutaharrik, S., Cerea, M., Foppoli, A., Maroni, A., Palugan, L., Zema, L., Gazzaniga, A., 2021. The chronotopic™ system for pulsatile and colonic delivery of active molecules in the era of precision medicine: feasibility by 3D printing via fused deposition modeling (FDM). Pharmaceutics 13, 759.
Micikas, R.J., Acharyya, A., Smith III, A.B., Gai, F., 2022. Synthesis and characterization of the fluorescence utility of two visible-light-absorbing tryptophan derivatives. Chem. Phys. Lett. 795, 139553.
Mondal, D.B., Velayudhan, J.M., Lekshman, A., Mandal, R.S.K., Raja, R., Kumar, N., 2022. Nanofabrication of catechin-loaded alginate, pectin, and chitosan polymeric nanoparticles. Tissue Scaffolds. Springer, pp. 399–422.
Nguyen, H.M., Morgan, H.W.T., Chantarojsiri, T., Kerr, T.A., Yang, J.Y., Alexandrova, A. N., Léonard, N.G., 2023. Charge and solvent effects on the redox behavior of vanadyl salen–crown complexes. J. Phys. Chem. A.
Parikh, T., Gupta, S.S., Meena, A., Serajuddin, A.T.M., 2016. Investigation of thermal and viscoelastic properties of polymers relevant to hot melt extrusion-III: Polymethacrylates and polymethacrylic acid based polymers. J. Excipients Food Chem. 5.
Pool, H., Luna-Barcenas, G., McClements, D.J., Mendoza, S., 2017. Development of polymethacrylate nanospheres as targeted delivery systems for catechin within the gastrointestinal tract. J. Nanoparticle Res. 19, 1–15.
Pool, H., Quintanar, D., de Dios Figueroa, J., Mano, C.M., Bechara, J.E.H., God\'\inez, L. A., Mendoza, S., 2012. Antioxidant effects of quercetin and catechin encapsulated into PLGA nanoparticles. J. Nanomater. 86, 2012.
Popova, M., Trendafilova, I., Zgureva, D., Kalvachev, Y., Boycheva, S., Novak Tušar, N., Szegedi, A., 2018. Polymer-coated mesoporous silica nanoparticles for controlled release of the prodrug sulfasalazine. J. Drug Deliv. Sci. Technol. 44, 415–420. https://doi.org/10.1016/j.jddst.2018.01.020.
Prakashkumar, N., Asik, R.M., Kavitha, T., Archunan, G., Suganthy, N., 2021. Unveiling the anticancer and antibiofilm potential of catechin overlaid reduced graphene oxide/zinc oxide nanocomposites. J. Clust. Sci. 1–18.
Pritam, P., Deka, R., Bhardwaj, A., Srivastava, R., Kumar, D., Jha, A.K., Jha, N.K., Villa, C., Jha, S.K., 2022. Antioxidants in Alzheimer's disease: current therapeutic significance and future prospects. Biology (Basel) 11, 212.
Qu, Z., Wong, K.Y., Moniruzzaman, M., Begun, J., Santos, H.A., Hasnain, S.Z., Kumeria, T., McGuckin, M.A., Popat, A., 2021. One-pot synthesis of ph-responsive eudragit-mesoporous silica nanocomposites enable colonic delivery of glucocorticoids for the treatment of inflammatory bowel disease. Adv. Ther. 4, 1–11. https://doi.org/10.1002/adtp.202000165.
Rahaman, S.N., Ayyadurai, N., Anandasadagopan, S.K., 2023. Synergistic effect of vancomycin and gallic acid loaded MCM-41 mesoporous silica nanoparticles for septic arthritis management. J. Drug Deliv. Sci. Technol. 82, 104353.
Rahman, I.A., Jafarzadeh, M., Sipaut, C.S., 2009. Synthesis of organo-functionalized nanosilica via a co-condensation modification using γ-aminopropyltriethoxysilane (APTES). Ceram. Int. 35, 1883–1888.
Rajan, M., Raj, V., Al-Arfaj, A.A., Murugan, A.M., 2013. Hyaluronidase enzyme core-5-fluorouracil-loaded chitosan-PEG-gelatin polymer nanocomposites as targeted and controlled drug delivery vehicles. Int. J. Pharm. 453, 514–522.
Rashidinejad, A., Birch, E.J., Sun-Waterhouse, D., Everett, D.W., 2014. Delivery of green tea catechin and epigallocatechin gallate in liposomes incorporated into low-fat hard cheese. Food Chem. 156, 176–183.
Raza, A., Sime, F.B., Cabot, P.J., Roberts, J.A., Falconer, J.R., Kumeria, T., Popat, A., 2021. Liquid CO2 formulated mesoporous silica nanoparticles for pH-responsive oral delivery of meropenem. ACS Biomater. Sci. Eng. 7, 1836–1853.
Rehman, S., Ranjha, N.M., Shoukat, H., Madni, A., Ahmad, F., Raza, M.R., Jameel, Q.A., Majeed, A., Ramzan, N., 2021. Fabrication, evaluation, in vivo pharmacokinetic and toxicological analysis of pH-sensitive eudragit S-100-coated hydrogel beads: a promising strategy for colon targeting. AAPS PharmSciTech 22, 1–17.
Salonen, J., Laitinen, L., Kaukonen, A.M., Tuura, J., Björkqvist, M., Heikkilä, T., Vähä-Heikkilä, K., Hirvonen, J., Lehto, V.P., 2005. Mesoporous silicon microparticles for oral drug delivery: loading and release of five model drugs. J. Control. Release 108, 362–374.
Sapino, S., Ugazio, E., Gastaldi, L., Miletto, I., Berlier, G., Zonari, D., Oliaro-Bosso, S., 2015. Mesoporous silica as topical nanocarriers for quercetin: characterization and in vitro studies. Eur. J. Pharm. Biopharm. 89, 116–125.
Saxena, I., Kumar, V., Gupta, A., 2023. An overview of molecular interaction studies of binary/ternary liquid mixtures with R4NI salts using ultrasonic velocity, transport, apparent molar volume, and dielectric constant properties. J. Solution Chem. 1–21.

Selestin Raja, I., Thangam, R., Fathima, N.N., 2018. Polymeric micelle of a gelatin-oleylamine conjugate: a prominent drug delivery carrier for treating triple negative breast cancer cells. ACS Appl. Bio Mater. 1, 1725–1734.
Shim, W., Kim, C.E., Lee, M., Lee, S.H., Park, J., Do, M., Yang, J., Lee, H., 2019. Catechin solubilization by spontaneous hydrogen bonding with poly (ethylene glycol) for dry eye therapeutics. J. Control. Release 307, 413–422.
Siepmann, J., Peppas, N.A., 2012. Modeling of drug release from delivery systems based on hydroxypropyl methylcellulose (HPMC). Adv. Drug Deliv. Rev. 64, 163–174.
Singh, N.A., Mandal, A.K.A., Khan, Z.A., 2017. Fabrication of PLA-PEG nanoparticles as delivery systems for improved stability and controlled release of catechin. J. Nanomater, 2017.
Sinsinwar, S., Vadivel, V., 2021. Development and characterization of catechin-in-cyclodextrin-in-phospholipid liposome to eradicate MRSA-mediated surgical site infection: investigation of their anti-infective efficacy through in vitro and in vivo studies. Int. J. Pharm. 609, 121130.
Sistanipour, E., Meshkini, A., Oveisi, H., 2018. Catechin-conjugated mesoporous hydroxyapatite nanoparticle: a novel nano-antioxidant with enhanced osteogenic property. Colloids Surfaces B Biointerfaces 169, 329–339. https://doi.org/10.1016/j.colsurfb.2018.05.046.
Subramanian, P., 2021. Lipid-based nanocarrier system for the effective delivery of nutraceuticals. Molecules 26, 5510.
Subudhi, M.B., Jain, Ankit, Jain, Ashish, Hurkat, P., Shilpi, S., Gulbake, A., Jain, S.K., 2015. Eudragit S100 coated citrus pectin nanoparticles for colon targeting of 5-fluorouracil. Materials (Basel) 8, 832–849.
Suner, S.S., Sahiner, M., Mohapatra, S., Ayyala, R.S., Bhethanabotla, V.R., Sahiner, N., 2022. Degradable poly(catechin) nanoparticles as a versatile therapeutic agent. Int. J. Polym. Mater. Polym. Biomater. 71, 1104–1115. https://doi.org/10.1080/00914037.2021.1941957.
Sunoqrot, S., Abujamous, L., 2019. pH-sensitive polymeric nanoparticles of quercetin as a potential colon cancer-targeted nanomedicine. J. Drug Deliv. Sci. Technol. 52, 670–676.
Sunoqrot, S., Al-Bakri, A.G., Ibrahim, L.H., Aldaken, N., 2022. Amphotericin B-loaded plant-inspired polyphenol nanoparticles enhance its antifungal activity and biocompatibility. ACS Appl. Bio Mater. 5, 5156–5164.
Vickers, N.J., 2017. Animal communication: when i'm calling you, will you answer too? Curr. Biol. 27, R713–R715.
Vong, C.I., Rathinasabapathy, T., Moncada, M., Komarnytsky, S., 2022. All polyphenols are not created equal: exploring the diversity of phenolic metabolites. J. Agric. Food Chem. 70, 2077–2091.
Wei, G., Li, J., Yan, M., Wang, C., 2016. Surface modification of MSNs with β-CD and use as a drug delivery system. Mater. Technol. 31, 482–486.
Wijewantha, N., Sane, S., Eikanger, M., Antony, R.M., Potts, R.A., Lang, L., Rezvani, K., Sereda, G., 2023. Enhancing anti-tumorigenic efficacy of eugenol in human colon cancer cells using enzyme-responsive nanoparticles. Cancers (Basel) 15, 1145.
Xu, H., Luo, R., Dong, L., Pu, X., Chen, Q., Ye, N., Qi, S., Han, X., Nie, W., Fu, C., others, 2022. pH/ROS dual-sensitive and chondroitin sulfate wrapped poly (β-amino ester)-SA-PAPE copolymer nanoparticles for macrophage-targeted oral therapy for ulcerative colitis. Nanomed. Nanotechnol. Biol. Med. 39, 102461.
Yaneva, Z., Ivanova, D., Popov, N., 2021. Clinoptilolite microparticles as carriers of catechin-rich acacia catechu extracts: microencapsulation and in vitro release study. Molecules 26, 1–19. https://doi.org/10.3390/molecules26061655.
Yuvakkumar, R., Elango, V., Rajendran, V., Kannan, N., 2014. High-purity nano silica powder from rice husk using a simple chemical method. J. Exp. Nanosci. 9, 272–281.
Zafar, S., Arshad, M.S., Rana, S.J., Patel, M., Yousef, B., Ahmad, Z., 2023. Engineering of clarithromycin loaded stimulus responsive dissolving microneedle patches for the treatment of biofilms. Int. J. Pharm. 640, 123003.
Zhang, G., Han, W., Zhao, P., Wang, Z., Li, M., Sui, X., Liu, Y., Tian, B., He, Z., Fu, Q., 2023. Programmed pH-responsive core-shell nanoparticles for precisely targeted therapy of ulcerative colitis. Nanoscale.
Zhang, X., Zhu, Y., Fan, L., Ling, J., Yang, L.Y., Wang, N., Ouyang, X., 2022. Delivery of curcumin by fucoidan-coated mesoporous silica nanoparticles: fabrication, characterization, and in vitro release performance. Int. J. Biol. Macromol.
Zhang, Y., Zhi, Z., Jiang, T., Zhang, J., Wang, Z., Wang, S., 2010. Spherical mesoporous silica nanoparticles for loading and release of the poorly water-soluble drug telmisartan. J. Control. Release 145, 257–263.
Zhao, J., Yang, J., Xie, Y., 2019. Improvement strategies for the oral bioavailability of poorly water-soluble flavonoids: an overview. Int. J. Pharm. 570, 118642.
Zhou, S., Zhong, Q., Wang, Y., Hu, P., Zhong, W., Huang, C.B., Yu, Z.Q., Ding, C.D., Liu, H., Fu, J., 2022. Chemically engineered mesoporous silica nanoparticles-based intelligent delivery systems for theranostic applications in multiple cancerous/non-cancerous diseases. Coord. Chem. Rev. 452, 214309.